© 2020. Published by The Company of Biologists Ltd | Journal of Cell Science (2020) 133, jcs237982. doi:10.1242/jcs.237982

RESEARCH ARTICLE

The cell polarity proteins Boi1 and Boi2 direct an actin nucleation complex to sites of exocytosis in *Saccharomyces cerevisiae*

Oliver Glomb[1], Yehui Wu[1], Lucia Rieger[1], Diana Rüthnick[2], Medhanie A. Mulaw[3] and Nils Johnsson[1,*]

ABSTRACT

Owing to the local enrichment of factors that influence its dynamics and organization, the actin cytoskeleton displays different shapes and functions within the same cell. In yeast cells, post-Golgi vesicles ride on long actin cables to the bud tip. The proteins Boi1 and Boi2 (Boi1/2) participate in tethering and docking these vesicles to the plasma membrane. Here, we show in *Saccharomyces cerevisiae* that Boi1/2 also recruit nucleation and elongation factors to form actin filaments at sites of exocytosis. Disrupting the connection between Boi1/2 and the nucleation factor Bud6 impairs filament formation, reduces the directed movement of the vesicles to the tip and shortens the vesicles' tethering time at the cortex. Transplanting Boi1 from the bud tip to the peroxisomal membrane partially redirects the actin cytoskeleton and the vesicular flow towards the peroxisome, and creates an alternative, rudimentary vesicle-docking zone. We conclude that Boi1/2, through interactions with Bud6 and Bni1, induce the formation of a cortical actin structure that receives and aligns incoming vesicles before fusion with the membrane.

KEY WORDS: Polar growth, Vesicular traffic, Actin nucleation, Cdc42, Split-Ubiquitin, Yeast

INTRODUCTION

The directed transport of post-Golgi vesicles influences the shape of cells and forms diverse structures such as axons in animals, hyphal extensions in fungi or pollen tubes in plants. Polar growth is the result of a conserved and complex interplay between RhoGTPase-based signaling, cytoskeletal organization, and vesicular traffic and fusion. By growing exclusively through budding, yeast serves as a model organism to understand the molecular mechanisms behind polar growth (Bi and Park, 2012). The bud tip of yeast cells is the site of preferred exocytosis and hosts a complex assembly of proteins that tether secretory vesicles to the plasma membrane. These vesicles arrive on actin cables at the tip by a myosin type V (Myo2)-driven transport (Donovan and Bretscher, 2012, 2015). Myo2 is anchored to the vesicles by binding to the membrane-bound RabGTPase Sec4 and to Sec15, a member of the exocyst (Jin et al., 2011). The exocyst is an eight-membered complex belonging to the CATCHR family of protein receptors that adsorb vesicles to the membranes of their target organelles. The exocyst is bound to the vesicle and activated by $Sec4_{GTP}$ (Guo et al., 1999). Upon arrival at the cortex of the tip, the exocyst attaches the vesicle to the membrane and initiates the formation of the docking complex (Boyd et al., 2004; Guo et al., 1999; He et al., 2007; Yue et al., 2017). The minimal bridge between vesicle and plasma membrane consists of plasma membrane-bound t-SNAREs, vesicle-bound v-SNAREs and the SM protein Sec1 (Hashizume et al., 2009; Morgera et al., 2012). Fusion is achieved by rearrangements of the docking complex that drive the two membranes into close apposition (Sudhof and Rothman, 2009).

The polar direction of the vesicular flow and the formation of a vesicle tethering and docking zone at its receiving are regulated by the small GTPase Cdc42. Control is exerted at least on three levels. First, linear actin cables that point to the bud tip are formed by the nucleation-promoting factor Bud6 in cooperation with the formin Bni1 (Amberg et al., 1997; Graziano et al., 2011; Moseley et al., 2004). Bud6 and Bni1 colocalize at the tip of the bud as members of the polarisome multi-protein complex (Amberg et al., 1997; Sheu et al., 1998). Full activation of this complex requires the binding of small RhoGTPases to relieve the auto-inhibition of Bni1 (Evangelista et al., 1997; Li and Higgs, 2003, 2005).

Second, Cdc42 binds to the exocyst members Sec3 and Exo70, and contributes directly to the localization and activation of the exocyst (Wu et al., 2010; Yamashita et al., 2010; Zhang et al., 2001). Finally, $Cdc42_{GTP}$ binds to the scaffold protein Bem1 and the paralogous polarity proteins Boi1 and Boi2 (Bender et al., 1996). Bem1, and Boi1 and Boi2 (hereafter referred to as Boi1/2) form a complex at the cortex that recruits the Cdc42 guanine nucleotide exchange factor Cdc24, and several members of the exocyst complex (Bender et al., 1996; Kustermann et al., 2017; Liu and Novick, 2014). The C-terminal PH domains of Boi1/2 interact with phospholipids and Sec1 (Kustermann et al., 2017). These interactions were proposed to participate in vesicle tethering and the assembly of the docking complex. Consequently, the deletion of Boi1/2 leads to a massive accumulation of post-Golgi vesicle in the bud (Kustermann et al., 2017; Masgrau et al., 2017).

With vesicle diameters of 70–100 nm, each fusion alters the lipid and protein composition of the plasma membrane. The estimated consumption of one vesicle per 3 s should continuously dilute polarity and tethering factors at the tip by enlarging the membrane surface (Donovan and Bretscher, 2012). How a directional persistency of tip direct flow and vesicle fusion is maintained under these conditions remains an open question. Post-Golgi vesicles do not fuse with the plasma membrane immediately upon arrival, but stay immobile for a defined time at or close by the site of their prospective fusion. This dwell time depends, among other factors, on the vesicle-bound Myo2 and thus on the presence of an actin structure adjacent to the site of fusion (Donovan and Bretscher, 2015). It is thus possible that members of the tethering and docking machinery are linked to the cortex and might even stimulate the outgrowth of actin filament to attract the incoming vesicles to the sites of previous fusions.

[1]Institute of Molecular Genetics and Cell Biology, Department of Biology, Ulm University, James-Franck-Ring N27, D-89081 Ulm, Germany. [2]ZMBH, University of Heidelberg, Im Neuenheimer Feld 282, D-69120 Heidelberg, Germany. [3]Comprehensive Cancer Center Ulm, Institute of Experimental Cancer Research, Ulm University, James-Franck-Ring N27, D-89081 Ulm, Germany.

*Author for correspondence (nils.johnsson@uni-ulm.de)

O.G., 0000-0002-1762-5037; L.R., 0000-0001-9521-8683; M.A.M., 0000-0002-2501-6952; N.J., 0000-0003-1416-835X

Received 14 August 2019; Accepted 19 December 2019

Journal of Cell Science (2020) 133, jcs237982. doi:10.1242/jcs.237982

Deletion of core components of the polarisome dissolves the focused distribution of Bud6 and Bni1, yet leaves actin filament formation and the delivery of vesicles less tip directed but otherwise still largely intact (Tcheperegine et al., 2005). This finding suggests the existence of additional factors that direct filament formation towards the membrane of the bud. We describe a complex consisting of Bud6, Bni1 and the vesicle-tethering factors Boi1 and Boi2, which initiates the formation of actin filaments at or close to the sites of vesicle fusion.

RESULTS

Boi1/2 physically interact with actin nucleation and elongation factors

To identify alternative regulators of actin filament nucleation in the bud, we performed a systematic Split-Ubiquitin (Split-Ub) interaction analysis and screened Bni1 and Bud6 as C_{ub}–RUra3 fusions (CRU) against an array of 504 N_{ub} fusion proteins. The array was enriched in proteins involved in the actin cytoskeleton, vesicular trafficking and other activities of polar cell growth (Hruby et al., 2011; Johnsson and Varshavsky, 1994; Wittke et al., 1999). The Split-Ub analysis revealed specific binding partners for Bni1 or Bud6, and binding partners that interacted with both proteins (Fig. 1A; Fig. S1, Table S1). Among those were Boi1 and Boi2, two homologous proteins that perform overlapping functions in the tethering and fusion of post-Golgi vesicles at the plasma membrane (Kustermann et al., 2017; Masgrau et al., 2017). As vesicles travel along actin cables to the membrane, a better understanding of the interaction between Boi1/2 and the actin nucleation complex might reveal how cable formation might be regulated at sites of exocytosis. Boi1 and Boi2 were already shown to interact with Bud6 *in vivo* (Kustermann et al., 2017). As Boi1 and Boi2 perform their essential functions redundantly, we focused our molecular analysis predominantly on Boi1.

Split-Ub interaction analysis in strains lacking either *BUD6* or *BNI1* confirmed that both proteins interact independently of each other with Boi1, whereas N_{ub} fusions to the negative controls Tdh1, Guk1 and Kel1 showed no interactions (Fig. 1B–E). N_{ub} fusions to fragments of Boi1 or Boi2 localized the binding sites for Bud6 and Bni1 to their N-terminal 300 residues (Fig. 1C). Split-Ub analysis of CRU fusions to fragments of Bni1 placed the binding site for Boi1 within the N-terminal 854 residues of Bni1 and thus away from the C-terminally located binding site for Bud6 (Fig. 1D) (Moseley and Goode, 2005). N_{ub} fusions to fragments of Bud6 confined the Boi1 interaction site to the N-terminal 141 residues of Bud6 (Fig. 1E). We expressed the so-defined minimal binding fragments of Boi1 (1–203), Bud6 (1–141) and Bni1 (1–854) in *Escherichia coli* and could show by pull-down analysis that the interaction between Boi1 and Bni1, and that between Boi1 and Bud6, is direct (Fig. 1F). To obtain a mutation that disrupts the interaction to Bud6 without grossly disturbing the structure of Boi1, we further fine mapped the Bud6 interaction site on Boi1. A screen of N_{ub} fusions to different N-terminal fragments of Boi1 identified the linker region (residues 77–178) between the SRC homology 3 (SH3) domain and the sterile alpha motif (SAM) domain as an autonomous binding site for Bud6 (Fig. S2). A pull down of the purified His-tagged $Bud6_{1–141}$ with a glutathione S-transferase (GST) fusion to $Boi_{77–178}$ confirmed our analysis (Fig. S2). We deleted the Boi1-linker region in the yeast genome ($boi1_{\Delta86–178}$) and tested the $Boi1_{\Delta86–178}$CRU-expressing strain against the N_{ub} array, and the N_{ub} fusion to $Boi1_{\Delta86–178}$ against Bud6CRU and Bni1CRU. Both analyses confirmed that $Boi1_{\Delta86–178}$ had specifically lost its interaction with Bud6 (Fig. 1G,H). The interactions with other polarity proteins such as Bem1 and Sec1 remained unaffected by this deletion (Fig. 1G; Fig. S2). Importantly, the deletion did not detectably impair the interaction between Boi1 and Bni1 (Fig. 1H).

Overexpressing Boi1–mCherry leads to large unbudded cells in which the plasma membrane is decorated by Boi1–mCherry (Fig. 1J) (Bender et al., 1996). Visualizing the actin structures in these cells with Lifeact, or co-expressing GFP fusions to Bud6 or Bni1, shows that all three proteins relocate to the Boi1–mCherry-stained cortex. This observation provides the first indication that Boi1 might bind to the Bni1–Bud6 complex in its active actin filament-promoting conformation (Fig. 1I,J).

The Boi proteins influence the actin cytoskeleton independently of their vesicle fusion activity

Our experiments suggest that Boi1/2 might guide the Bni1–Bud6 complex to generate actin filaments at sites of exocytosis. To corroborate our hypothesis we visualized the actin cytoskeleton in *boi1Δboi2Δ* cells expressing fragments of Boi1 of increasing length (Fig. 2A). The C-terminal PH domain of Boi1 is the minimal fragment that rescues the essential function of Boi1/2 during vesicle fusion (Kustermann et al., 2017). Cells expressing this domain ($boi1_{\Delta414}$ *boi2Δ*) were significantly enriched in delocalized actin patches and appeared to contain fewer and thinner actin cables than the corresponding *boi2Δ* cells (Fig. 2A,B). This effect documents a clear impact of Boi1/2 on the actin cytoskeleton. We next correlated the presence of the Bud6 and Bni1 binding sites on the expressed Boi1 fragments with changes of the actin cytoskeleton in these cells. A deletion of the first 203 residues removes the major Bud6 binding site of Boi1 and strongly affects the binding to Bni1 (Fig. 1C). This deletion already reduced the percentage of actin cables and also increased the amount of delocalized actin patches (Fig. 2A,B). Additionally, removing the SAM domain of Boi1 ($boi1_{\Delta299}$) and thus any residual interactions with Bni1 further lowered the amount of actin cables and enhanced the number of delocalized actin patches to similar levels to those found in cells expressing only $boi1_{\Delta414}$ (Figs 1C and 2A,B). The impaired vesicle fusion of a *boi1Δboi2Δ* strain can be suppressed by overexpression of the t-SNARE Sso1 (Kustermann et al., 2017). The still-disorganized actin structure of this strain confirms that actin organization and vesicle docking are distinct activities of Boi1/2 (Fig. 2A,B). A GFP fusion to the RabGTPase Sec4 is a marker for post-Golgi vesicles, which become highly polarized in the growing bud (Jin et al., 2011). Truncating Boi1 from its N-terminus increasingly dissolved the tip-focused distribution of these vesicles (Fig. 2A,C). This observation further substantiates the role of Boi1/2 in actin organization as secretory vesicles strictly travel on actin cables (Pruyne et al., 1998).

The Boi1–Bud6 complex stimulates actin filament formation in the bud

The high density of actin patches interferes with the simultaneous detection of actin cables in the bud. We thus repeated the actin staining of *boi2Δ* cells carrying the minimally perturbed $boi1_{\Delta86–178}$ allele after treatment with the actin patch inhibitor CK-666 (Hetrick et al., 2013). Structured illumination microscopy (SIM) of the actin cytoskeleton showed that the bud of $boi1_{\Delta86–178}$*boi2Δ* cells was less densely filled with actin cables than that of *boi2Δ* cells (Fig. 2D). By applying the coefficient of variation (COV) as a quantitative measure of actin cable density, we could support the conclusion derived from the visual inspection of the cells (Fig. 2E) (Garabedian et al., 2018) (see Materials and Methods). Compared to wild-type and *boi2Δ* cells, $boi1_{\Delta86–178}$ *boi2Δ* cells also displayed fewer actin

Journal of Cell Science (2020) 133, jcs237982. doi:10.1242/jcs.237982

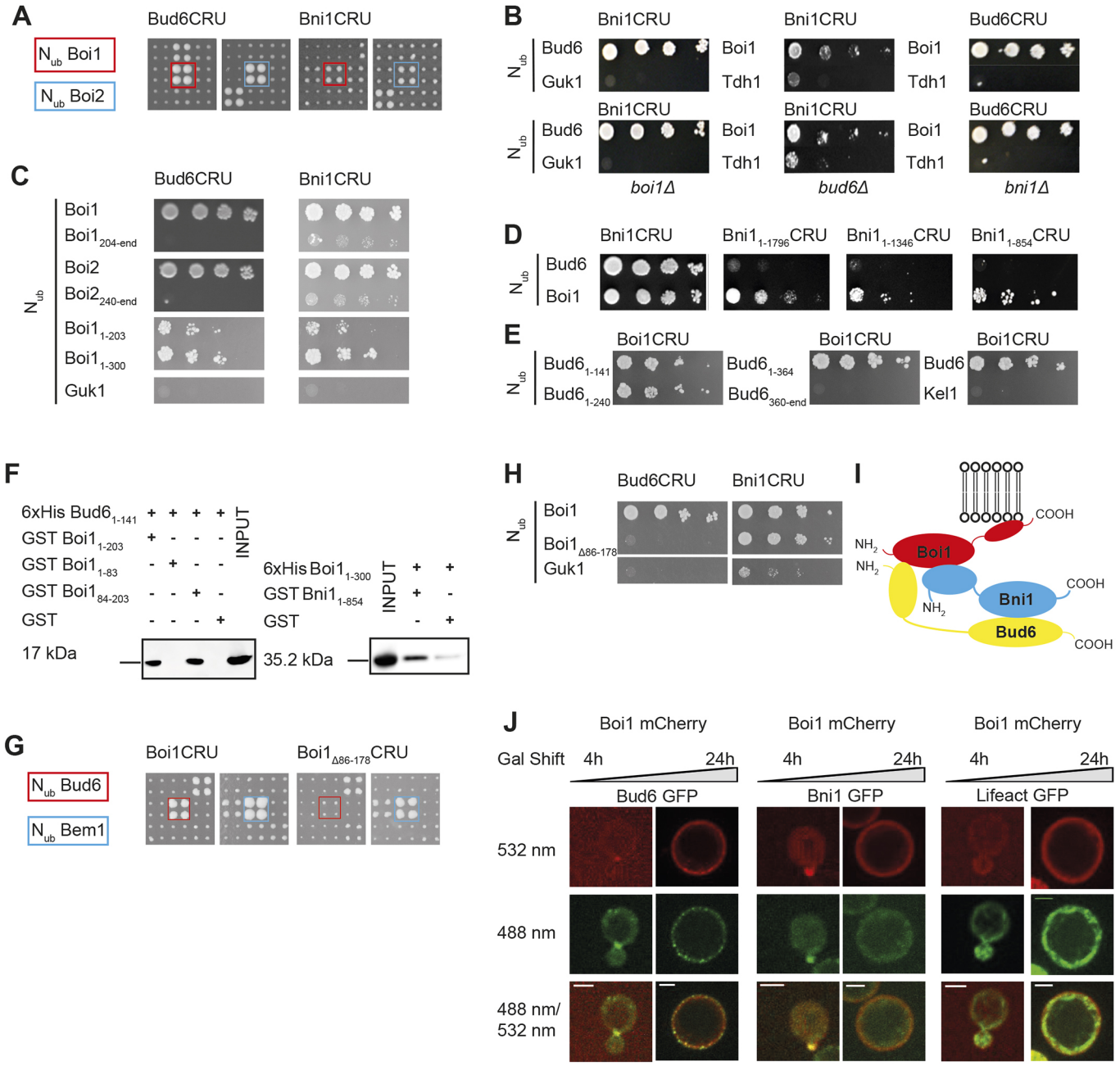

Fig. 1. Boi1/2 interact with Bud6 and Bni1. (A) Cut-outs of a Split-Ub array of diploid yeast cells containing Bud6CRU (left) or Bni1CRU (right), and co-expressing different N_{ub} fusions. The N_{ub}- and CRU-expressing cells were independently mated four times, spotted in quadruplets and transferred onto medium containing 5-FOA. Growth of four colonies indicates interaction. N_{ub}–Boi1 and N_{ub}-Boi2 are highlighted in red and blue, respectively (see Fig. S1 for the complete array and Table S1 for a list of interaction partners). (B) 4 µl of yeast cultures co-expressing the indicated N_{ub} and C_{ub} fusion proteins were spotted in 10-fold serial dilutions, starting with an OD_{600} of 1, on medium containing 5-FOA. N_{ub} fusions to Guk1 or Tdh1 were used as negative controls. Top row shows the interactions in otherwise wild-type yeast. Bottom row shows interactions in the absence of *BOI1* (left), *BUD6* (middle) or *BNI1* (right). (C) As in B, but with cells co-expressing Bud6CRU (left) or Bni1CRU (right) and the indicated fragments of Boi1 or Boi2 as N_{ub} fusions. (D) As in B, but with cells co-expressing N_{ub}–Boi1 or N_{ub}–Bud6 and C-terminally truncated fragments of Bni1 as CRU fusions. (E) As in B, but with cells co-expressing Boi1CRU together with Bud6 or fragments of Bud6 as N_{ub} fusions. N_{ub}–Kel1 served as a negative control. (F) Extracts of *E. coli* cells expressing 6xHis fusion of $Bud6_{1–141}$ (left) or $Boi1_{1–300}$ (right) were incubated with sepharose beads exposing GST, or GST fusions to fragments of Boi1 (left) or Bni1 (right). Input (left blot, rightmost lane; right blot, leftmost lane) and bound fractions were separated by SDS–PAGE and analyzed by anti-His antibodies after transfer onto nitrocellulose. Corresponding SDS–PAGE and quantification of the western blots are provided in Fig. S2A–C. (G) As in A, but with cells expressing Boi1CRU or $Boi1_{Δ86–178}$CRU. Interactions of N_{ub}–Bud6 and N_{ub}–Bem1 are highlighted in red and blue, respectively (see Fig. S2 for complete arrays). Bud6 does not interact with $Boi1_{Δ86–178}$. (H) As in B, but with cells co-expressing Bud6CRU (left) or Bni1CRU (right) with the indicated N_{ub} fusions. $Boi1_{Δ86–178}$ still interacts with Bni1. (I) Hypothetical model of the Bud6–Boi1–Bni1 complex summarizing the *in vivo* and *in vitro* interaction data. The interaction between Bud6 and Bni1 has been extensively studied by others (Graziano et al., 2011; Tu et al., 2012). The simultaneous binding of Bud6 and Bni1 to Boi1 remains to be proven (see Discussion section). (J) Yeast cells containing P_{GAL1}*–BOI1–mCherry* and co-expressing either Bud6–GFP, Bni1–GFP or Lifeact were shifted to galactose for 4 h (left columns in panels) and 24 h (right columns in panels) to induce overexpression of Boi1–mCherry. Shown are the mCherry channel (top row), the GFP channel (middle row) and the overlay of both channels (bottom row). All the GFP fusions are recruited to the cortex upon Boi1 overexpression. Scale bars: 2 µm.

Journal of Cell Science (2020) 133, jcs237982. doi:10.1242/jcs.237982

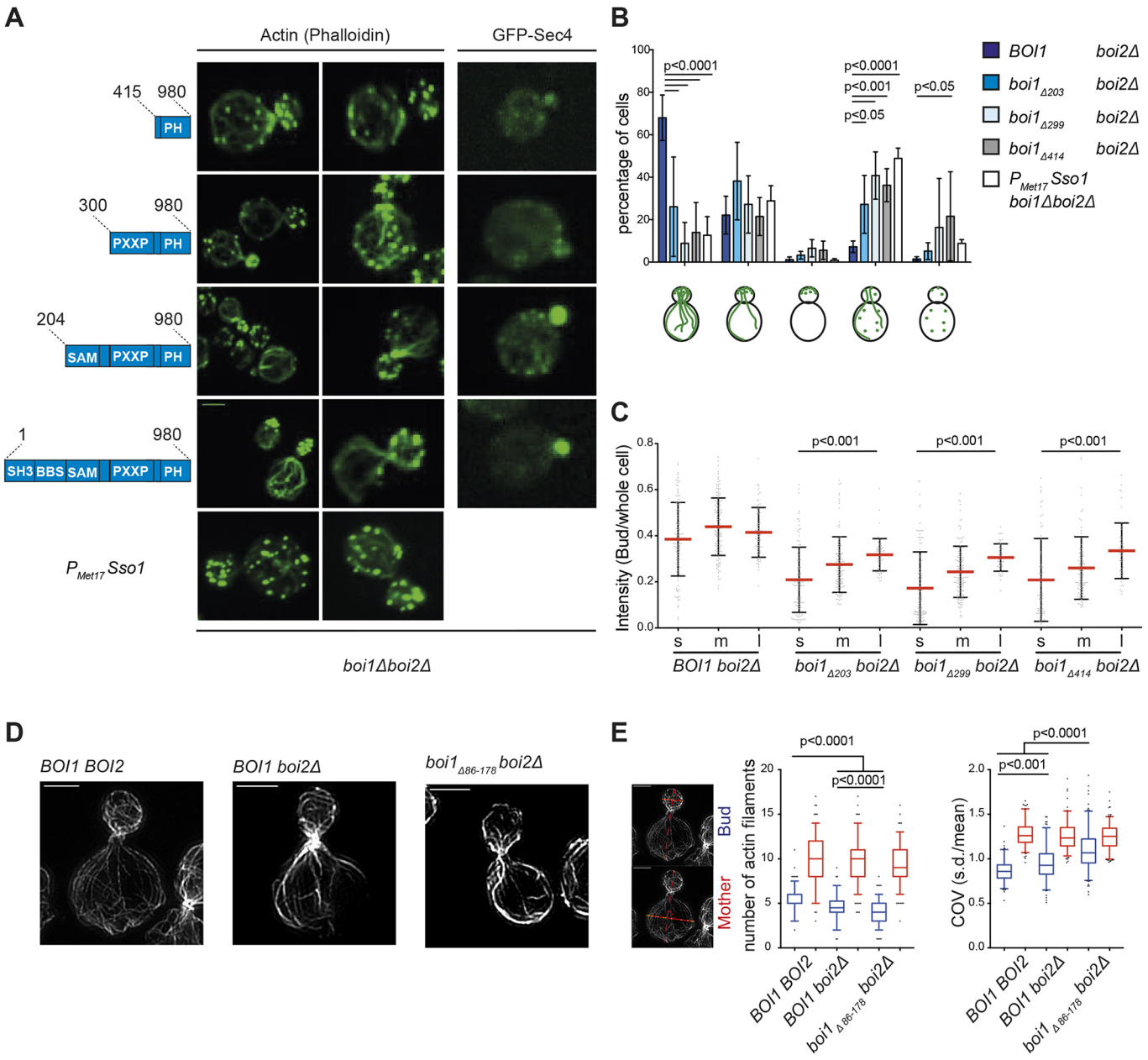

Fig. 2. Mutations in Boi1 influence the actin cytoskeleton. (A) Fluorescence microscopy of *boi2Δ* cells expressing different, genomically integrated fragments of *BOI1* under a copper-inducible promoter after staining actin with Alexa Fluor 488–phalloidin (left and middle columns), or co-expressing GFP–Sec4 as a marker for post-Golgi vesicles (right column). Scale bar: 2 µm. (B) Quantification of actin phenotypes of cells in A, according to the categories as shown by the cartoons below the chart (from left to right: wild-type cells, few and seemingly thinner actin cables, no actin cables, few actin cables and mislocalized actin patches, no actin cables and mislocalized actin patches). Analysis was based on three independent experiments with in total $n_{BOI1,\ boi2\Delta}$=642, $n_{boi1\Delta203,\ boi2\Delta}$=823, $n_{boi1\Delta299,\ boi2\Delta}$=333, $n_{boi1\Delta414,\ boi2\Delta}$=666 and $n_{PMET17–SSo1boi1\Delta414,\ boi2\Delta}$=257 cells. Statistical analysis was performed with a two-way ANOVA using a Tukey's post-test for multiple comparisons. (C) The ratio of the GFP–Sec4 intensities of the bud to the whole cell were used to quantify the degree of polarized secretory vesicles in small (s, <1.5 µm), medium (m, 1.5–3 µm) and large buds (l, >3 µm) of the cells in A. The buds were binned according to their length. The experiments were performed in duplicate with two clones analyzed for each genotype, resulting in a total cell number of $n_{BOI1,\ boi2\Delta}$=114 (s), 135 (m), 63 (l); $n_{boi1\Delta203,\ boi2\Delta}$=107 (s), 118 (m), 65 (l); $n_{boi1\Delta299,\ boi2\Delta}$=101 (s), 133 (m), 52 (l); $n_{boi1\Delta414,\ boi2\Delta}$=68 (s), 103 (m), 51 (l). Statistical analysis with calculated *P*-values are based on a non-parametric Kruskal–Wallis test followed by Dunn's post-test for multiple comparisons. (D) Representative SIM images of cells treated with 1 µM CK-666 for 10 min and stained with Alexa Fluor 488–phalloidin. Scale bars: 2 µm. (E) SIM images of in total $n_{BOI1,\ BOI2}$=149 (tip), 175 (mother); $n_{BOI1,\ boi2\Delta}$=150 (tip), 199 (mother); $n_{boi1\Delta86\text{-}178,\ boi2\Delta}$=169 (tip), 220 (mother) cells analyzed from three independent measurements to quantify the number of actin cables crossing a virtual plane in the bud (blue) and mother cell (red) (left and middle). Middle: Shown are the distributions of the numbers of filaments per cell. Right: In total, $n_{BOI1,\ BOI2}$=123 (tip, mother), $n_{BOI1,\ boi2\Delta}$=135 (tip, mother) and $n_{boi1\Delta86–178,\ boi2\Delta}$=167 (tip, mother) cells were taken to measure the actin cable densities. COV, coefficient of variation. Statistical analysis was performed with a Kruskal–Wallis test followed by Dunn's post-test for multiple comparisons. All error bars show the s.d of the mean.

cables crossing a virtual plane that was placed in the bud perpendicular to the polarity axis (Fig. 2E). In contrast, actin filament number and density were not changed in mother cells upon deletion of the Bud6 binding site in Boi1 (Fig. 2E). The polar localization of Bud6 was not affected in *boi1*$_{\Delta86–178}$ *boi2Δ* cells (Fig. S3).

Journal of Cell Science (2020) 133, jcs237982. doi:10.1242/jcs.237982

Cortical actin modulates vesicular flow and fusion

To measure the influence of the Boi1/2-induced actin structures on the movement and fusion of post-Golgi vesicles, we photobleached the buds of cells expressing GFP–Sec4 and compared the trajectories of individual vesicles entering the bud of wild-type, *boi2Δ* and *boi1*$_{\Delta 86–178}$ *boi2Δ* cells by time-lapse microscopy (Movie 1) (Donovan and Bretscher, 2015). Incoming vesicles in wild-type cells were often directly transported to the cell cortex, where they either tethered and subsequently fused, or moved along the cortex to the tip, where fusion occurred. Incoming vesicles in *boi2Δ* cells took longer to find their final destinations, and this was more pronounced in *boi1*$_{\Delta 86–178}$ *boi2Δ* cells (Movie 1). In particular, post-Golgi vesicles in *boi1*$_{\Delta 86–178}$ *boi2Δ* cells headed after their first contact with the cortex to a different region of the cortex or tumbled within the center of the bud. We occasionally observed an incoming vesicle that was redirected to the mother cell after shortly touching the cortex of the bud. Moreover, incoming vesicles seemed to reside longer at the neck before entering the bud (Movie 1).

To quantify the differences between the alleles, we measured the GFP–Sec4 fluorescence intensity of a small corridor adjacent to the plasma membrane of the bud and normalized it to the intensity of the whole bud (Fig. 3A). In wild-type cells, GFP–Sec4 was clearly restricted to the narrow zone beneath the plasma membrane. In *boi1*$_{\Delta 86–178}$ *boi2Δ* cells, GFP–Sec4 was more equally distributed throughout the bud. GFP–Sec4 was also slightly enriched at the bud neck of these cells (Fig. 3A).

Tracking individual post-Golgi vesicles is best achieved in medium-sized and large buds. To complement our tracking experiments, we observed GFP–Sec4 by SIM of fixed cells to look at the distribution of post-Golgi vesicles in small buds, where vesicular traffic is more tip directed. Vesicles stained the cortex in a very restricted zone at the tip of wild-type cells (Fig. 3B). This zone became slightly broader in *boi2*Δ cells (Fig. 3B). This trend continued in *boi1*$_{\Delta 86–178}$ *boi2*Δ cells in which the GFP–Sec4 staining also extended more toward the center of the bud and additionally appeared in small clusters at the bud neck (Fig. 3B).

Vesicles that reached their final destination at the cortex stayed there on average for 10.85 s before disappearing, most probably through fusion with the plasma membrane (Fig. 3C). The tethering time was significantly reduced to 7.7 s in *boi1*$_{\Delta 86–178}$ *Δboi2* cells. As *boi2*Δ cells displayed a near-wild-type tethering time of 10.5 s, we conclude that the impaired interaction between Bud6 and Boi1$_{\Delta 86–178}$ causes the faster fusion of vesicles with the plasma membrane (Fig. 3C).

Boi1/2 induce autonomous actin nucleation sites

The Boi1/2-independent location of Bud6, and the presence of Boi1/2-independent actin structures at the cortex, prevent us from unequivocally concluding from the experiment in Fig. 1J that a Boi1/2–Bud6–Bni1 complex initiates actin filaments *de novo* (Fig. S3). By fusing Boi1 to Pex3, a membrane protein of the peroxisomes, we aimed to remove Boi1 from the known actin nucleation centers of the bud to study its activity in isolation at the membrane of the peroxisome (Fig. 4A) (Luo et al., 2014). Pex3$_{1–45}$–mCherry–Boi1 (Pex–Boi1) is efficiently targeted to the membrane of the peroxisomes (Fig. 4B). By co-expressing a GFP fusion to proteins involved in polar growth including known ligands of Boi1/2, we could show that Boi1 attracts all its tested binding partners to the peroxisome including Bni1 and members of the exocyst (Fig. 4C,E; Fig. S4). In contrast, polarity proteins not known to directly bind to Boi1/2 (Ste20, Cla4, Rga1, Rga2) were not enriched at the Boi1-labeled peroxisomes (Fig. 4E; Fig. S4) (Kustermann et al., 2017). GFP–Cdc42 partially relocated to Boi1-labeled peroxisomes, whereas a GFP fusion to the Cdc42- and Rac-interactive binding (CRIB) domain of Gic2 (Gic2 CRIB), a probe to sense the GTP-bound form Cdc42, remained exclusively at the bud tip (Fig. 4E; Fig. S4) (Brown et al., 1997). Although indicative, the experiment cannot definitely exclude the presence of active Cdc42 at the Boi1-labeled peroxisomes, as a detection by Gic2 CRIB not only requires Cdc42$_{GTP}$ but also other features of the plasma membrane that might not be found at the peroxisome (Takahashi and Pryciak, 2007).

Actin staining revealed the establishment of an alternative axis of cell polarity in the Pex–Boi1-expressing cells (Fig. 4C,D). The actin cables of this alternative axis seem to emanate from peroxisomes located in the mother. To distinguish the contribution of the actin nucleation factors from the contributions of all other recruited proteins, we repeated the experiments with cells expressing peroxisome-targeted Boi1$_{\Delta 86–178}$ (Pex–Boi1$_{\Delta 86–178}$) lacking the binding site to Bud6. Accordingly, Bud6–GFP was no longer found at Pex–Boi1$_{\Delta 86–178}$-labeled peroxisomes. Bni1, Exo84, Sec3, Cdc24 and Bem1 bind Boi1 at a different site and consequently still colocalized with Pex–Boi1$_{\Delta 86–178}$-labelled peroxisomes (Figs 4C and 1H; Table S2). Actin cables in this strain were often less polarized towards the cell tip but did not any longer align towards the peroxisomes (Fig. 4C,D). A significant portion of cells still contained actin patches around peroxisomes (Fig. 4D).

We performed three additional experiments to better characterize the Boi1-generated actin structures around the peroxisomes. First, a GFP fusion to Bnr1, the bud neck-localized formin of *Saccharomyces cerevisiae*, is not enriched at Boi1-labeled peroxisomes (Fig. 5A,B). Second, a deletion of *BNI1* abrogates the activity of Boi1 to initiate actin structures around peroxisomes (Fig. 5C,D). Finally, incubation with CK-666 does not impair but slightly increases the generation of the actin cables from Boi1-labeled peroxisomes (Fig. 5E,F). All three features of the peroxisomal actin structure confirm its similarity to the actin structure formed at the tip of the cells.

Deleting the region between the N-terminal SH3 domain and the SAM domain in Pex–Boi1$_{\Delta 86–178}$ impairs the interaction with Bud6, and might also affect other activities of Boi1 (Fig. 1). To further support the existence of functional Bud6–Boi1–Bni1 complex at Boi1-labeled peroxisomes, we compared the formation of actin cables in Pex–Boi1-expressing *bud6*Δ cells containing ectopic copies of GFP–Bud6 or GFP–Bud6$_{360–end}$. In contrast to the full-length protein, GFP–Bud6$_{360–end}$, lacking the Boi1 binding site (Fig. 1E) but still being able to bind to actin and Bni1, failed to support the formation of actin structures at the peroxisomes (Fig. 5G,H) (Tu et al., 2012).

The GFP fusion of the v-SNARE Snc1 (GFP–Snc1) and Sec4 were enriched at the peroxisomes of Pex–Boi1- but not of Pex–Boi1$_{\Delta 86–178}$-expressing cells (Fig. 6A,B). As both GFP fusions are attached to post-Golgi vesicles, their recruitment to the peroxisome indicates the reconstitution of an at least partially functional vesicle-tethering zone. Consequently, Boi1- but not Boi1$_{\Delta 86–178}$-labeled peroxisomes, when found in close apposition to the plasma membrane, often induce an outward bulging of the cell wall (Figs 4C, 5C,E,G and 6A).

Tracking of individual GFP–Sec4-labeled post-Golgi vesicles confirmed the formation of an alternative and functional polarity axis (Fig. 6C,D,E; Movie 2). Cells containing Boi1-decorated peroxisomes displayed a reduced flux of vesicles to the bud (Fig. 6C,D). The reduction was partially compensated by an

Journal of Cell Science (2020) 133, jcs237982. doi:10.1242/jcs.237982

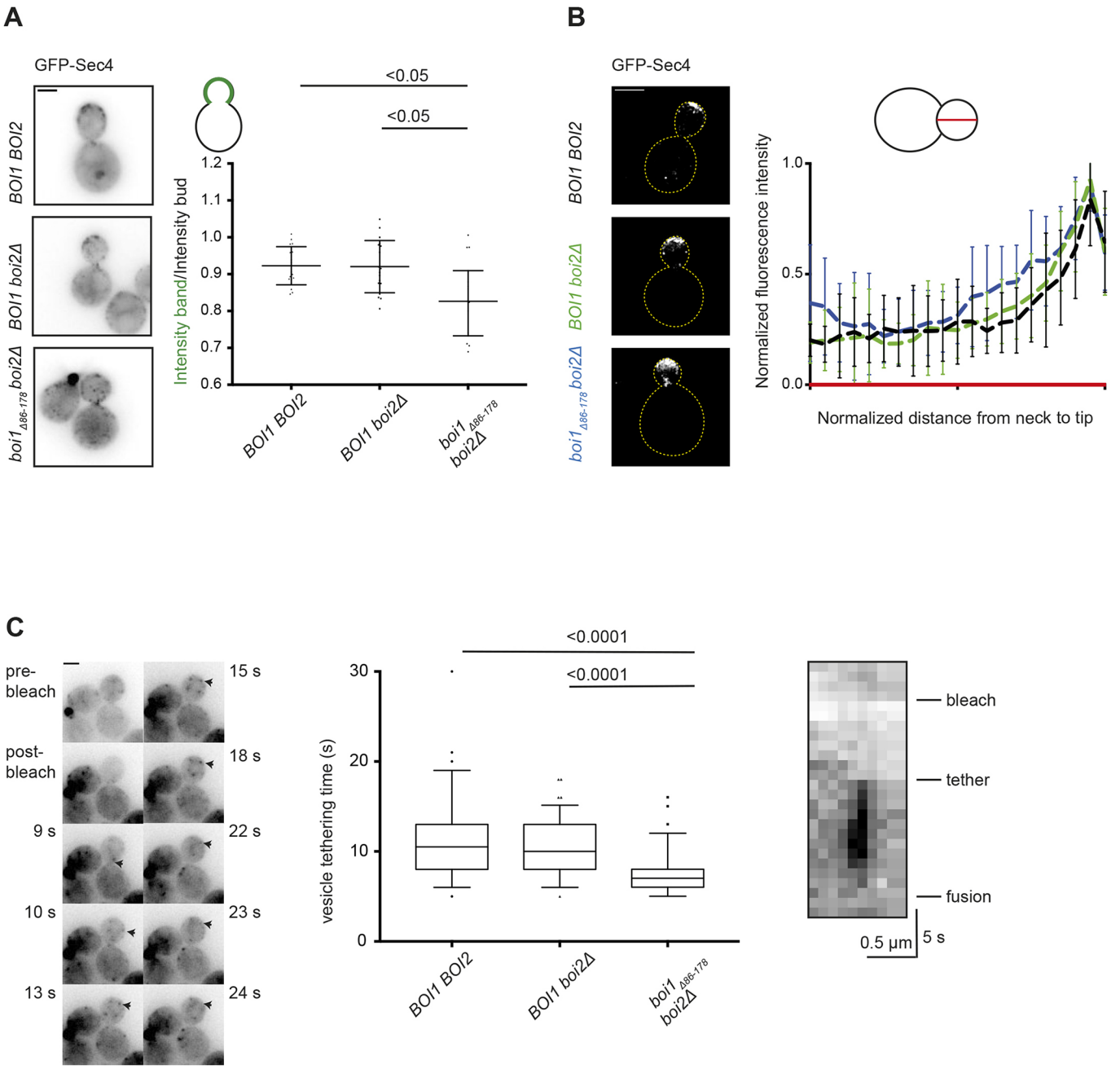

Fig. 3. The Boi1–Bud6 interaction is important for vesicle movement and tethering. (A) *BOI1 BOI2*, *BOI1 boi2*Δ and *boi1*$_{Δ86–178}$ *boi2*Δ cells expressing GFP–Sec4 were analyzed by time-lapse microscopy, taking an image of five stacks every 1 s over 104 frames. The bud was bleached after four frames to visualize incoming vesicles. Left: projections of the vesicle distribution of the complete time course. Right: ratios of mean intensities of a corridor below the plasma membrane representing the tethered and docked vesicles to the mean intensity of the entire bud. Error bars indicate the s.d. of the mean (n=15 from two independent experiments for all genotypes tested). Statistical analysis was performed with a Kruskal–Wallis test followed by Dunn's post-test. (B) *BOI1 BOI2*, *BOI1 boi2*Δ and *boi1*$_{Δ86–178}$ *boi2*Δ cells expressing GFP–Sec4 were fixed and visualized by SIM. Left: GFP–Sec4 distributions in cells of the indicated genotypes. Right: mean intensity profiles of GFP–Sec4 from the bud necks to the tips of ten cells per genotype (black, *BOI1 BOI2*; green, *BOI1 boi2*Δ; blue, *boi1*$_{Δ86–178}$ *boi2*Δ; five cells/measurement). All error bars show the s.d of the mean. (C) Determination of the vesicle-tethering time based on time-lapse microscopy from A. Left: fluorescence microscopy of a wild-type cell expressing GFP–Sec4, showing the movement, tethering and fusion of a vesicle in consecutive images. Middle: quantification of vesicle-tethering time based on two independent experiments with $n_{BOI1,\ BOI2}$=102, $n_{BOI1,\ boi2Δ}$=98, $n_{boi1Δ86–178,\ boi2Δ}$=96 vesicles measured in total. Statistical analysis is based on a Kruskal–Wallis test followed by Dunn's post-test. Right: kymograph used for the determination of the tethering time of the vesicle highlighted in the fluorescence microscopy images. Scale bars: 2 µm.

increase in the fraction of vesicles that moved away from the bud towards the Boi1-labeled peroxisomes (Fig. 6C,E). This redirection of vesicular traffic was not seen in cells expressing Pex–Boi1$_{Δ86–178}$ (Fig. 6C-E). The measured directional vesicular traffic was strictly actin dependent (Fig. 6F).

DISCUSSION

In most eukaryotic organisms, post-Golgi vesicles arrive at the cell plasma membrane through a directed long-distance walk on microtubules or actin cables. The vesicles are then handed over to the actin filaments underlying the cortex (Hume et al., 2011;

Journal of Cell Science (2020) 133, jcs237982. doi:10.1242/jcs.237982

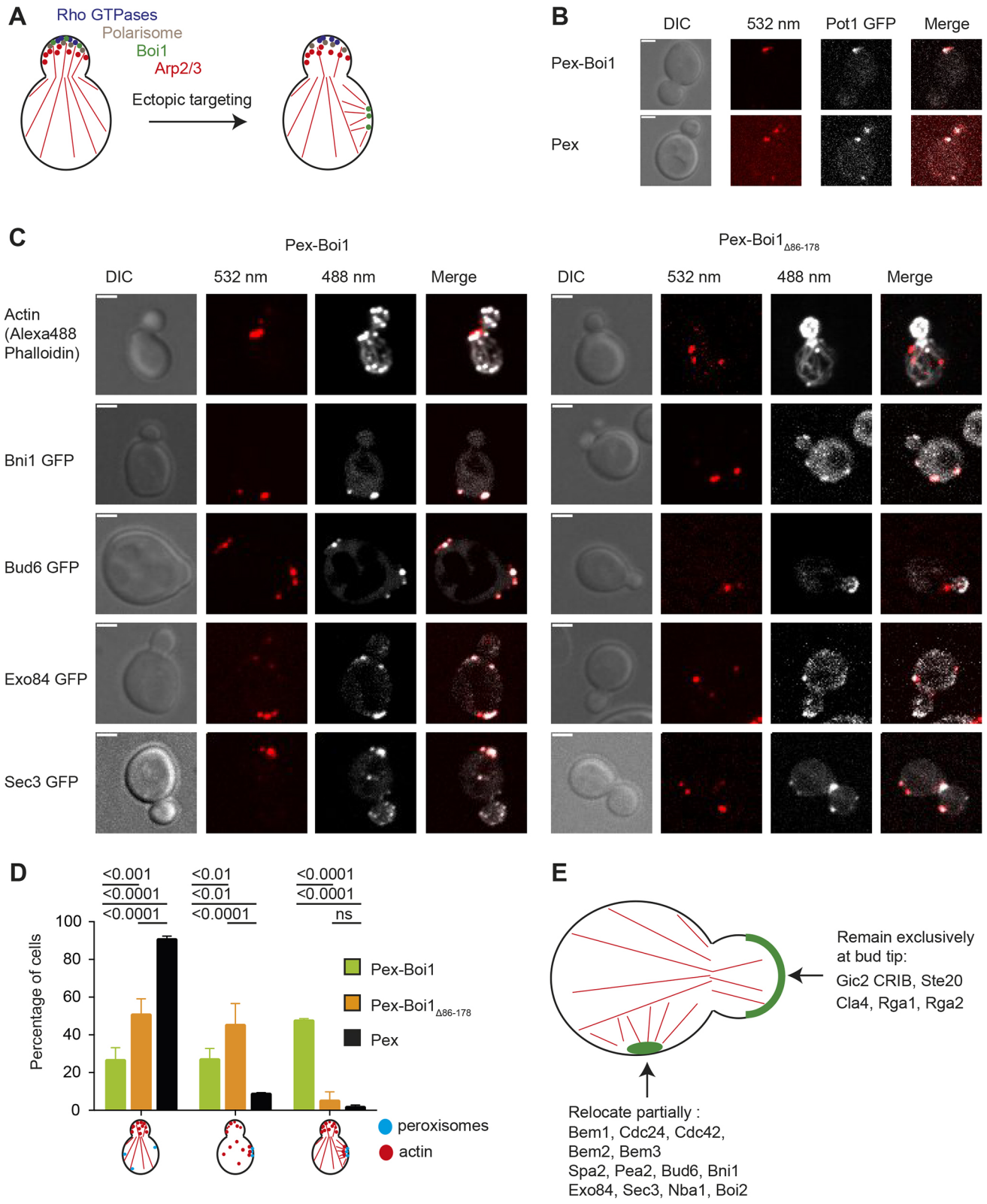

Fig. 4. See next page for legend.

Porat-Shliom et al., 2013). The actin-bound vesicles are either kept on hold during regulated exocytosis or processed directly for docking and fusion. In budding yeast, post-Golgi vesicles are transported exclusively on actin cables to the plasma membrane of the bud (Pruyne et al., 1998). We propose that in budding yeast, similar to other eukaryotes, secretory vesicles switch from actin cables used for long-distance transport to cortical actin filaments that guide the vesicle to the docking and fusion zone. Our

Journal of Cell Science (2020) 133, jcs237982. doi:10.1242/jcs.237982

Fig. 4. A Boi1–Bud6–Bni1 complex initiates actin filaments *de novo*. (A) Experimental design: $Pex3_{1–45}$–mCherry (Pex) was fused to Boi1 (Pex–Boi1) or to $Boi1_{\Delta86–178}$ (Pex–$Boi1_{\Delta86–178}$) to target the fusion to the peroxisome, allowing study of its actin nucleation activity in isolation from other nucleation factors in the bud. (B) Cells co-expressing the peroxisomal marker Pot1–GFP and Pex–Boi1 were visualized by confocal microscopy. Representative images show maximum projections of 10 *z*-stacks and a clear colocalization of both fusion proteins. (C) Fluorescence microscopy of cells co-expressing Pex–Boi1 or Pex–$Boi1_{\Delta86–178}$ together with GFP-labeled Bni1, Bud6, Exo84 or Sec3. Alexa Fluor 488–phalloidin staining visualized the actin cytoskeleton of these cells. Scale bars: 2 µm. (D) Phenotypic quantification of the actin cytoskeleton of cells expressing the indicated color-coded Pex fusions after Alexa Fluor 488–phalloidin staining. The categorization into three phenotypes is shown in the cartoons: (left) polarized actin cables and patches; (middle) mislocalized actin patches, partially colocalizing with peroxisomes; (right) bi-polar actin cable organization with filaments arising from peroxisomes. Data were derived from three independent actin stainings with in total $n_{Pex–Boi1}$=553, n_{Pex}=598, $n_{Pex–Boi1\Delta86–178}$=650 cells. Bars indicate the mean and error bars the s.d. Two-way ANOVA followed by a Tukey's multiple comparison test were used to determine the significance. ns, not significant. (E) Summary of the distributions of different GFP fusions in Pex–Boi1-expressing cells. A quantitative analysis of the distributions is shown in Table S2.

experiments point to Boi1/2 as contact sites for actin filament nucleation below the plasma membrane. Boi1/2 locate at the cortex and bind to Bud6 and the formin Bni1, two proteins that together form a potent actin nucleation and elongation complex (Graziano et al., 2011, 2013; Moseley and Goode, 2005). Abrogating the interaction between Boi1/2 and Bud6 reduces actin cable density in buds, increases the random movement of vesicles and shortens the tethering time of the bound vesicles. Furthermore, the artificial relocation of Boi1 to peroxisomes creates an alternative tethering zone at the peroxisome, including secretory vesicles and actin filaments that emanate from these sites. The zone is formed by the many binding partners of Boi1 and depends on the ability of Boi1 to recruit Bud6 and Bni1 to initiate actin cables (Fig. 7). The efficacy with which the peroxisome-tethered Boi1 competes with other factors in the cell for actin filament formation suggests that Boi1/2 not only anchors but also activates the Bni1–Bud6 complex upon binding. The architecture and stoichiometry of the Bud6–Boi1/2–Bni1 complex is unresolved. The cartoon in Fig. 1I is certainly an oversimplification as all three proteins form at least dimers, and Bni1 might also attach to Boi1 through its separate interaction with Bud6. The formation of a trimeric Bud6–Boi1–Bni1 complex is compatible with our experiments but other arrangements are at this point equally possible (Fig. 1I).

By focusing our analysis on the $boi1_{\Delta86–178}$ allele, we tried to separate its influence on actin filament formation from the protein's two other main functions, the localization of the Bem1–Cdc24 complex and the formation of the tethering and docking complex (Bender et al., 1996; Kustermann et al., 2017). The former activity is located on a short binding motif in the middle of the sequence of Boi1, whereas the latter activity locates on the membrane- and Sec1-binding C-terminal PH domain, and the Exo84-, Sec3-binding N-terminal SH3 domain (Kustermann et al., 2017). We propose that the concentration of all three activities in one protein coordinates vesicle fusion with trafficking and enables the control of both activities through RhoGTPases (Fig. 7A). Linking vesicle tethering and fusion with actin nucleation might foster vesicle docking at sites where fusion has recently occurred and thus equip secretion with the processivity that is required for polarized growth. Two alternative non-exclusive models that could explain processivity are shown in Fig. 7A and B. Binding to Bem1–Cdc24 might channel the activated Cdc42 through the $Cdc42_{GTP}$-binding PH domain of Boi1/2 to the exocyst components Sec3 and Exo70, and to the formin Bni1. As a consequence, vesicles are not only tethered to the membrane but mark the sites where new actin filaments will be generated (Fig. 7A) (Adamo et al., 2001; Guo et al., 1999, 2001; He et al., 2007; Morgera et al., 2012; Yue et al., 2017). Alternatively, Boi1/2-containing receptor complexes might generate actin filaments at the membrane that are used as stable tracks for multiple vesicles.

The reduction in vesicle-tethering time through the dissolution of the Boi1–Bud6 complex seems counterintuitive, yet might indicate that the cortical actin in yeast, as in higher eukaryotes, not only directs movement to the membrane but also restricts and controls the fusion of the vesicles with the plasma membrane (Li et al., 2018; Meunier and Gutiérrez, 2016). It was shown that the connection between Myo2 and the vesicles has to be dissolved before fusion can occur (Donovan and Bretscher, 2015). A reduced subcortical actin network might anchor Myo2 less rigidly at the cortex and thereby increase the chance of premature vesicle fusion. Our hypothesis is supported by the phenotypes of cells carrying a *BUD6* deletion. Here, the number of actin cables is reduced, but the velocity of post-Golgi vesicles, and the randomness of their movements, is increased. At the same time, exocytosis becomes less efficient in these cells (Jose et al., 2015).

Although budding yeast uses only actin structures for transport and docking, the significance of our findings is not restricted to these cells. Studies in neuroendocrine cells showed that the role of the cortical actin cytoskeleton is quite similar with respect to the coordination of exocytosis, where it also directs vesicular flow, and mediates docking and fusion (Chasserot-Golaz et al., 2005; Gabel et al., 2015). Upon stimulation, actin-associated proteins like the actin-bundling protein annexin A2 are targeted to the SNARE complex at the plasma membrane to reorganize the integrity of the cortical actin cytoskeleton and generate a vesicle fusion-promoting environment (Gabel et al., 2015; Umbrecht-Jenck et al., 2010).

The fission yeast *Schizosaccharomyces pombe* transports post-Golgi vesicles on microtubules. Deletion of its single Boi1/2 homolog Pop1 leads to the accumulation of secretory vesicles in the cytosol (Nakano et al., 2011). Pop1 was also shown to bind to the *S. pombe* formin For1. Disrupting this interaction disturbs the actin cytoskeleton (Rincón et al., 2009). Pop1 complements the essential function of Boi1/2 in vesicle fusion (Kustermann et al., 2017). These findings indicate that the molecules and mechanisms involved in the transfer of secretory vesicles from their long-distance carrier to cortical actin structures are quite conserved.

MATERIALS AND METHODS

Growth conditions and cultivation of strains

All yeast strains in this study are derivatives of the *S. cerevisiae* JD47 strain. Cells were incubated at 30°C in yeast extract peptone dextrose (YPD) or synthetic medium lacking specific amino acids, or complemented with antibiotics for selection. *E. coli* XL1 blue cells were used for plasmid amplification and grown at 37°C in lysogeny broth (LB) medium containing antibiotics. *E. coli* BL21 cells were used for protein production and were grown in LB or super broth (SB) medium at 37°C or 18°C.

Construction of plasmids and strains

Detailed lists of all primers, plasmids and strains from this study are provided in Tables S3, S4 and S5. Fusions of GFP or CRU to *BUD6*, *BNI1*, *BOI1* or $boi1_{\Delta86-178}$ were constructed by PCR amplification from genomic DNA of the respective C-terminal open-reading frames (ORFs) without stop codon as described (Dünkler et al., 2012; Wittke et al., 1999). The obtained DNA fragments were cloned via EagI and SalI restriction sites in front of the

Journal of Cell Science (2020) 133, jcs237982. doi:10.1242/jcs.237982

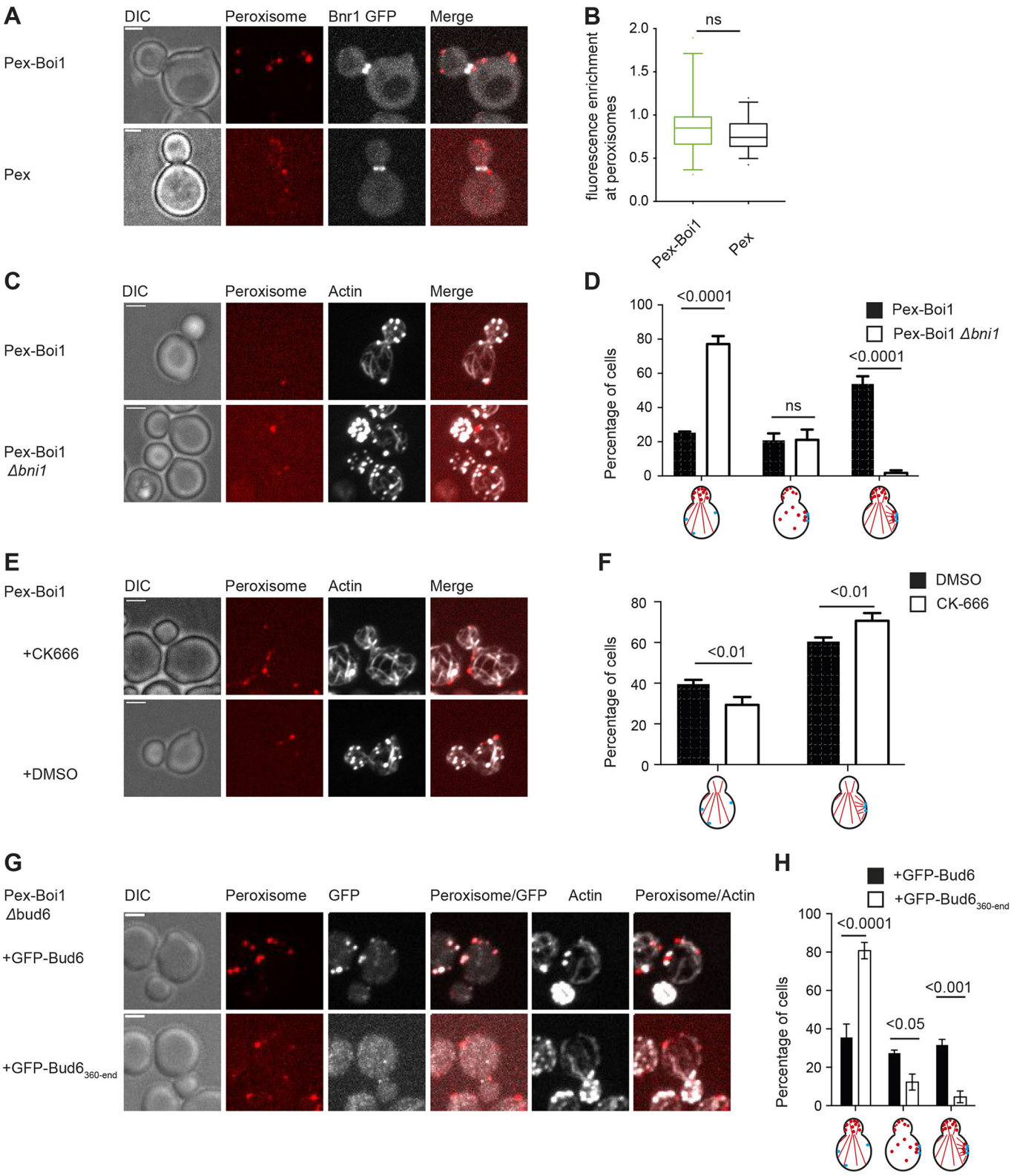

Fig. 5. See next page for legend.

CRU, GFP or mCherry module on a pRS303, pRS304 or pRS306 vector (Sikorski and Hieter, 1989). For integration into the genome, the plasmids were linearized using a single restriction site within the C-terminal genomic DNA sequence. Successful integration was verified by PCR of single yeast colonies with diagnostic primer combinations using a forward primer annealing in the target ORF, but upstream of the linearization site, and a reverse primer annealing in the C-terminal module. Gene deletions were obtained by replacing the ORF with an antibiotic resistance cassette through single-step homologous recombination as described (Janke et al., 2004). Genomic N_{ub} fusions were obtained as described (Hruby et al., 2011). Generation of yeast centromeric plasmids containing N_{ub} fusion proteins included initial PCR amplification of indicated fragments from genomic

Fig. 5. Actin polymerization from Boi1-decorated peroxisomes resembles filament formation at the bud tip. (A) Bnr1 is not detected at Boi1-decorated peroxisomes. Fluorescence microscopic images of *boi1Δ* cells expressing Bnr1–GFP and co-expressing Pex–Boi1 or Pex. Images show maximum projections of ten focal layers. (B) The relative fluorescence enrichment of Bnr1–GFP at Pex–Boi1/Pex-decorated peroxisomes relative to the cytosol was quantified in 30 yeast cells from A, derived from two independent experiments. Box plots with 5% to 95% whiskers are shown. Statistical significance was evaluated with a Mann–Whitney test. ns, not significant. (C) Actin polymerization from Boi1-decorated peroxisomes depends on Bni1. *boi1Δ or boi1Δbni1Δ* cells expressing Pex–Boi1 were stained with Alexa Fluor 488–phalloidin to visualize actin. The maximum projections of 14 stacked focal planes are shown. (D) Quantification of the actin cytoskeleton of cells shown in C, according to three phenotypes: (left) polarized actin cables and patches or mislocalized patches that do not colocalize with peroxisomes; (middle) mislocalized actin patches, partially colocalizing with peroxisomes; (right) bi-polar actin cable organization with filaments arising from peroxisomes. Data are derived from three independent actin stainings within total $n_{\text{Pex–Boi1},boi1\Delta}$=333, $n_{\text{Pex–Boi1},boi1\Delta bni1\Delta}$=381 cells. (E) Inhibition of Arp2/3 activity does not affect actin polymerization from Boi1-decorated peroxisomes. *boi1Δ* cells were incubated with 100 µM CK-666 or 0.1% dimethyl sulfoxide (DMSO) for 10 min followed by Alexa Fluor 488–phalloidin staining of the actin cytoskeleton. (F) Quantification of the actin cytoskeleton of cells shown in E, according to two phenotypes: (left) polarized actin cable or (right) bi-polar actin cable organization. Data are derived from three independent actin stainings with in total n_{DMSO}=270 and $n_{\text{CK-666}}$=576 cells.
(G) Actin polymerization from Boi1-decorated peroxisomes depends on Bud6. *boi1Δbud6Δ* cells expressing Pex–Boi1 and co-expressing either P_{BUD6}GFP–Bud6 or P_{BUD6}GFP–$Bud6_{360–end}$ were stained with Alexa Fluor 647–phalloidin to visualize actin. (H) Phenotypic quantification of cells shown in G, as in D. Data are derived from three independent actin stainings with in total $n_{\text{GFP–Bud6}}$=543 and $n_{\text{GFP–Bud6360–end}}$=398 cells. In D, F and H, bars indicate s.d. Significance was tested by two-way ANOVA followed by a Bonferroni multiple comparison test. Scale bars: 2 µm.

DNA containing a SalI restriction site in the forward primer and Acc65I restriction site in the reverse primer, digestion and ligation into the plasmid *N_{ub}-empty kanMX4*.

Fragments of *BUD6*, *BNI1* or *BOI1* were expressed as GST or 6xHis fusions in *E. coli* BL21. GST fusions were obtained by amplification of the respective fragments from genomic yeast DNA using primers containing NcoI or EcoRI restriction sites. The PCR fragments were cloned in-frame behind GST in the plasmid pGex6P1 or pGex2T (GE Healthcare, Buckinghamshire, UK). For 6xHis-tagged fragments, a PCR of the respective fragment from genomic DNA using primers containing SfiI restriction sites was performed, and the product was inserted in-frame downstream of a 6xHis tag into the pAC plasmid (Schneider et al., 2013). The chimeric $Pex3_{1–45}$–mCherry pRS306 plasmid was adapted from Luo et al. (2014). *BOI1* or *$boi1_{\Delta 86–178}$* were amplified from genomic DNA and inserted in-frame behind the mCherry tag using BamHI or SalI restriction sites.

Genomic integration of the *$boi1_{\Delta 86–178}$* allele was performed by 'delitto perfetto' methodology or CRISPR-Cas9 (Laughery et al., 2015; Storici and Resnick, 2006). The successful deletion and exchange of amino acids were confirmed by sequencing of single-colony PCRs. A detailed description of the construction of all plasmids can be obtained upon request.

In vitro binding assays

Protein expression

Overnight cultures of *E. coli* BL21 cells were diluted to an optical density at a wavelength of 600 nm (OD_{600}) of 0.3, and incubated at 37°C in LB or SB medium to an OD_{600} of 0.8 before protein synthesis was induced by the addition of isopropyl β-d-1-thiogalactopyranoside (IPTG). Protein expression conditions were optimized for each expression construct (Table S6). Cell pellets were stored after induction at −80°C.

Cell extract preparation

Cell pellets were resuspended in 1× PBS or 1× HBSEP (pH 7.4, 10 mM Hepes, 150 mM NaCl, 3 mM EDTA, 0.005% Tween 20) containing 1× protease inhibitor cocktail (Roche Diagnostics, Penzberg, Germany), incubated for 20 min with 1 mg/ml lysozyme on ice, and subsequently subjected to sonification for 2×4 min with a Bandelin Sonapuls HD 2070 (Reichmann Industrieservice, Hagen, Germany). Lysates were spun down at 40,000 ***g*** for 10 min at 4°C. Supernatants were transferred either directly to the binding assay or used for further purification.

Binding assay

All incubation steps were carried out under rotation in the cold room. Extracts of GST or GST fusion proteins were incubated for 0.5–1 h with glutathione-coated sepharose beads (GE Healthcare, Freiburg, Germany) equilibrated in PBS (Boi1–Bni1) or HBSEP (Boi1–Bud6). Beads were washed twice and incubated with 0.1 mg/ml bovine serum albumin (BSA) (Boi1–Bni1) (Sigma Chemicals, St Louis, MO) for 30 min, before the beads were treated with either purified 2 µM 6xHis $Bud6_{1–141}$, or extract of 6xHis $Boi1_{1–300}$ in the presence of 0.1 mg/ml BSA for 1 h. Beads were washed 3× with HBSEP or PBS before eluting the bound protein with 1× GST elution buffer (pH 8.0, 50 mM Tris, 20 mM reduced glutathione). Protein eluates were separated by SDS–PAGE and stained with Coomassie Brilliant Blue or with anti-His antibody after transfer onto a nitrocellulose membrane (Sigma-Aldrich, Steinheim, Germany; 1:5000).

Quantification of western blots

Western blots were quantified with ImageJ. A detailed step-by-step procedure is provided in https://di.uq.edu.au/community-and-alumni/sparq-ed/sparq-ed-services/using-imagej-quantify-blots. Briefly, the histogram of the intensities of each band of a western blot was used to calculate the area under the curve (AUC), which correlates to the size and brightness of each band. The AUC of each band was normalized to the AUC of the input band to quantitatively compare the amount of bound 6xHis-tagged fusion protein in each lane of the gel.

Protein purification

For purification of 6xHis–$Bud6_{1–141}$, cell pellets were extracted as above in 1× IMAC binding buffer (pH 7.5, 300 mM NaCl, 50 mM KH_2PO_4, 20 mM imidazole). Purification was achieved by immobilized metal affinity purification followed by size exclusion chromatography on an ÄktaPurifier Chromatography System (GE Healthcare, Buckinghamshire, UK).

The final protein concentration was determined with a NanoDrop ND-1000 spectral photometer (Peqlab, Erlangen, Germany) at 280 nm excitation, and based on a calculated excitation coefficient of 8.5 mM^{-1} cm^{-1} and a molecular mass of 17.7 kDa (www.expasy.org). The purified protein was used directly for pull-down analysis or stored at −20°C.

In vivo interaction analysis with the Split-Ub system

For Split-Ub array analysis, a library of 533 α-strains each expressing a different N_{ub} fusion were mated with a Bni1CRU-, Bud6CRU-, Boi1CRU- or $Boi1_{\Delta 86–178}$CRU-expressing α-strain. Diploids were transferred as independent quadruplets on synthetic defined (SD) medium containing 1 mg/ml 5-fluoroorotic acid (5-FOA), and different concentrations of copper to adjust the expression of the N_{ub} fusions (Fig. S1) (Dünkler et al., 2012). For individual Split-Ub interaction analysis, CRU- and N_{ub}-expressing strains were mated or co-expressed in haploid cells, and spotted onto medium containing 1 mg/ml 5-FOA and different concentrations of copper in four 10-fold serial dilutions starting from an OD_{600} of 1. Growth at 30°C was recorded every day for 2–5 days.

Microscopy

Wide-field and confocal microscopy

Fluorescence microscopy was performed on an Axio Observer Z.1 spinning-disc confocal microscope (Zeiss, Göttingen, Germany) containing a switchable Evolve512 EMCCD (Photometrics, Tucson, AZ), or an Axiocam Mrm camera (Zeiss). The microscope was also equipped with a Plan-Apochromat 100×/1.4 NA oil differential interference contrast (DIC) objective, and 488, 561 and 635 nm diode lasers (Zeiss). Images were recorded with the Zen2 software (Zeiss) and analyzed with FIJI [version

Journal of Cell Science (2020) 133, jcs237982. doi:10.1242/jcs.237982

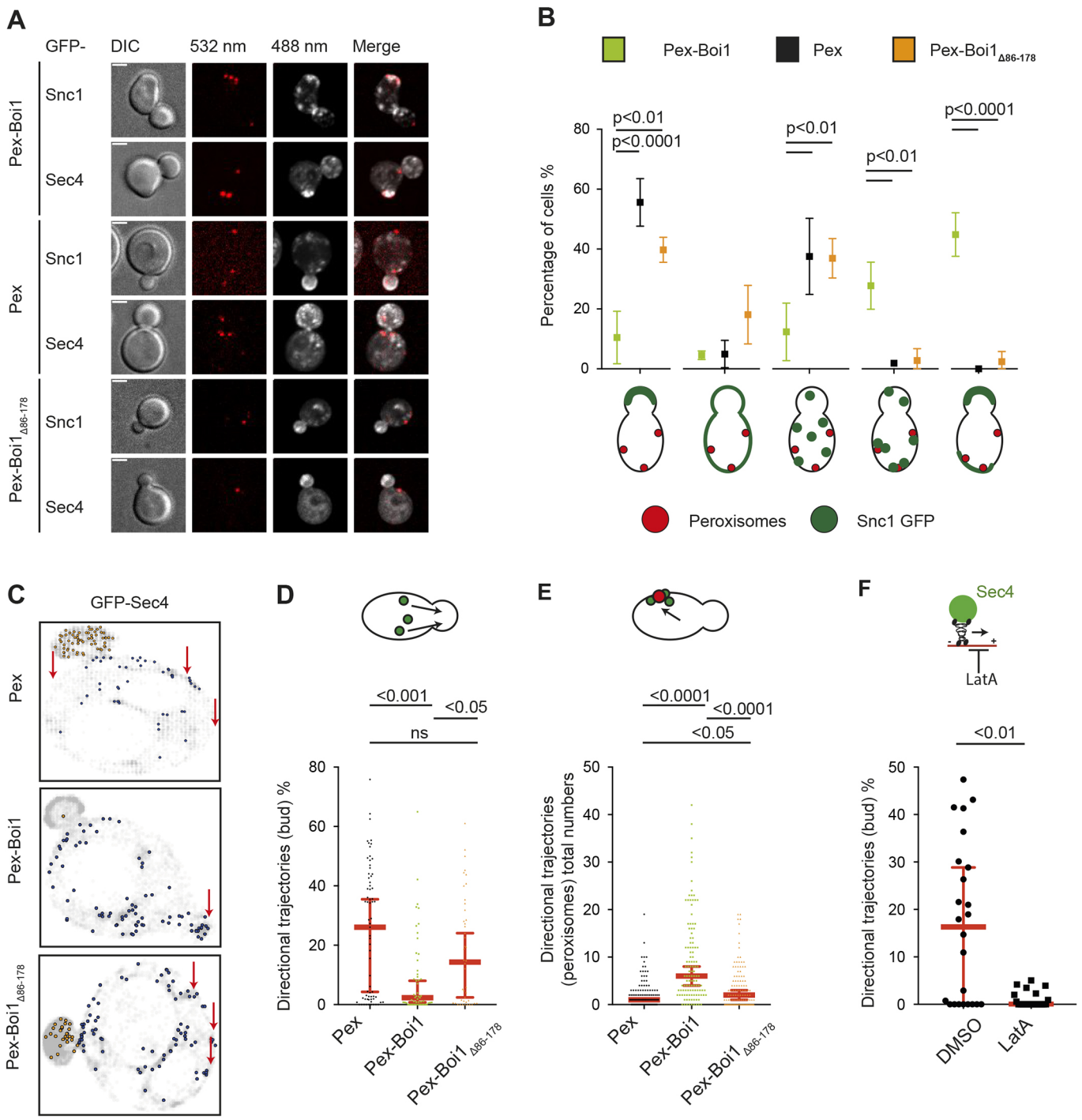

Fig. 6. Pex–Boi1 redirects the flow of post-Golgi vesicles to peroxisomes. (A) Representative images of cells co-expressing GFP–Sec4, or the v-SNARE GFP–Snc1 and either Pex–Boi1, Pex–Boi1$_{\Delta86–178}$ or Pex. Scale bars: 2 µm. (B) Quantification of GFP–Snc1 distributions in cells from A [Pex–Boi1 (green), Pex–Boi1$_{\Delta86–178}$ (orange), Pex (black)]. Distributions were categorized according to the cartoons below the chart. The experiments were performed twice with in total $n_{Pex–Boi1}$=177, n_{Pex}=107, $n_{Pex–Boi1\Delta86–178}$=221 cells. Statistical analysis was performed with a two-way ANOVA and Tukey's multiple comparison post-test. Error bars indicate s.d. of the mean. (C) *boi1Δ* cells co-expressing Pex–mCherry, Pex–Boi1 or Pex–Boi1$_{\Delta86–178}$ together with GFP–Sec4 were visualized by confocal microscopy. After bleaching the bud, images were taken every 100 ms over 35 s to follow the movement of the labeled vesicles. Shown are single cells of each genotype displaying the destinations of all vesicles. Vesicles moving into the bud are in orange, vesicles showing directional movement into the mother are in blue, and the remaining vesicles displaying no or random movements are in gray. Red arrows indicate the position of the peroxisomes. (D,E) Quantification of vesicle trajectories of cells shown in C. (D) Fraction of trajectories of vesicles moving into the bud of *boi1Δ* cells expressing the indicated Pex3 fusions. Black, Pex3–mCherry (n=69 cells); green, Pex–Boi1 (n=53 cells); orange, Pex–Boi1$_{\Delta86–178}$ (n=44 cells). (E) Number of directional trajectories/cell of vesicles moving towards the peroxisomes displaying the indicated Pex3 fusions. Black, Pex3$_{1–45}$–mCherry (n=132); green, Pex–Boi1 (n=117); orange, Pex–Boi1$_{\Delta86–178}$ (n=114). Data in D and E were collected from three independent measurements. Statistical analysis was performed with a Kruskal–Wallis test followed by Dunn's post-test. (F) Directed movements of the vesicles are strictly actin dependent. Cells co-expressing Pex3–mCherry and GFP–Sec4 were treated with 100 µM LatA or DMSO (control). Images of a single plane were taken every 100 ms over 35 s. The percentages of directionally transported vesicles entering the bud were calculated using 24 DMSO-treated, and 22 LatA-treated, cells from two independent experiments. Statistical comparison was performed with a Mann–Whitney test.

Journal of Cell Science (2020) 133, jcs237982. doi:10.1242/jcs.237982

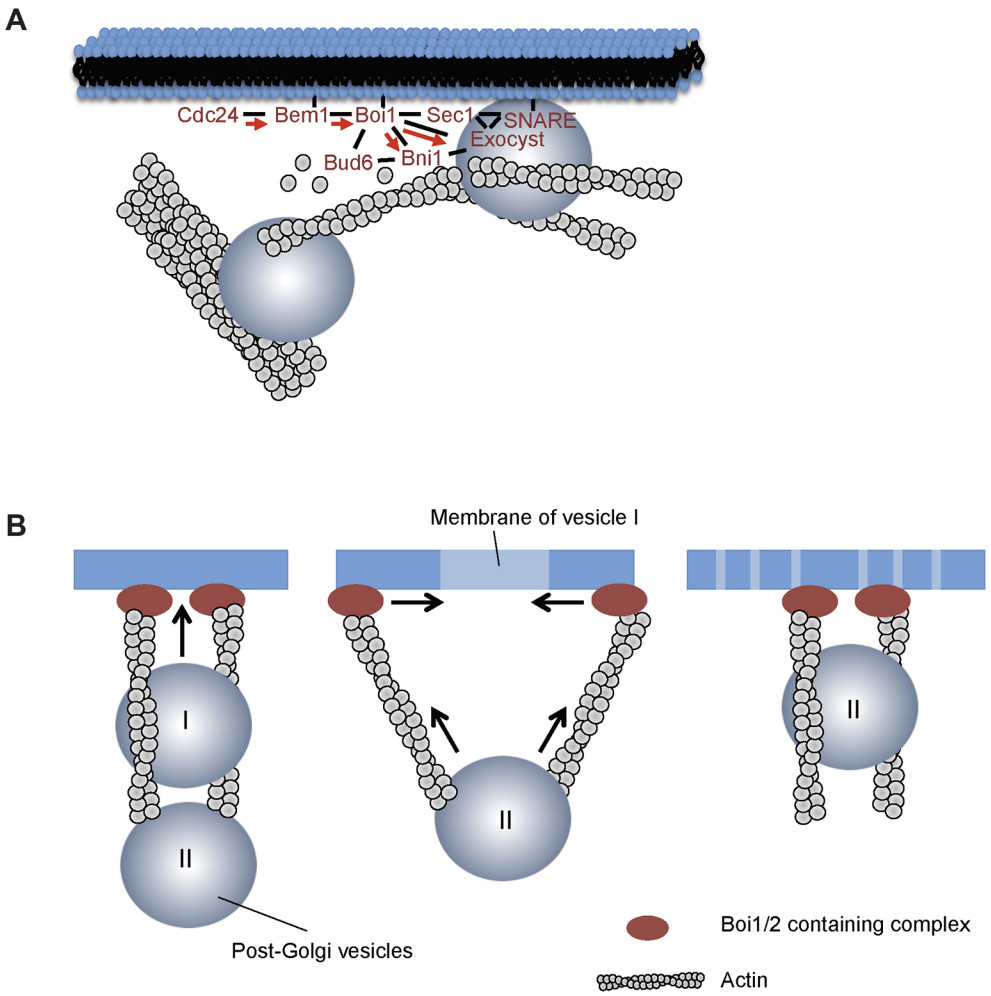

Fig. 7. The Boi proteins as hubs of polarized secretion and actin filament nucleation. (A) Boi1 binds through its PH domain to the plasma membrane of the bud and anchors, together with phospholipids, the Bem1–Cdc24 complex to the membrane. Cdc24 activates Cdc42, which is shuttled (red arrows) through Bem1 and Boi1 to its effectors. Boi1 contacts the exocyst and the SM protein Sec1 to prepare the vesicle for SNARE-mediated fusion. Simultaneously, the Boi1-bound Bud6–Bni1 complex initiates and elongates filaments to attract the next post-Golgi vesicle. Through their association with the actin cortex, Boi1/2 and their binding partners keep their position at the membrane. (B) The Boi1/2-containing receptor complexes generate actin filaments that serve as tracks for incoming vesicles. Upon fusion, the membrane of the vesicle I inserts into the plasma membrane and dilutes the receptor complexes. The actin filaments that emanate from the Boi1/2-containing receptors are already connected to the next vesicle (II) so that its Myo2-driven transport contracts the receptors to their original position. This movement provides directional persistency of the vesicle fusion process.

2.0.0-rc-69; National Institutes of Health (NIH) (Schindelin et al., 2012)]. Alternatively, time-lapse microscopy was performed with a DeltaVision system (GE Healthcare, Freiburg, Germany) provided with an Olympus IX71 wide-field microscope (Olympus, Hamburg, Germany). This microscope contained a CoolSNAP HQ2-ICX285 or a Cascade II 512 EMCCD camera (Photometrics), a 100× UPlanSApo 100×/1.4 NA oil ∞/0.17/FN26.5 objective (Olympus, Münster, Germany), a steady-state heating chamber and a Photofluor LM-75 halogen lamp (89 NORTH, ChromaTechnology, Williston, ND).

Secretory vesicles in the bud tip were observed with an iMIC microscope (Photonics, Pitsfield, MA) equipped with an Andor-Clara camera (Type Clara DR 328G-C01-SIL CCD), an oligochrome, a light-emitting diode (LED) camera with excitation filters FF01-340/26-25, FF01-387/11-25 and FF01-470/22-25, and a 60× oil Olympus ApoN 60×/1.490 NA oil ∞/0.13–0.19 objective. The microscope was controlled with the software Live Acquisition (v.2.6.0.34) (FEI Munich, Gräfelfing, Germany). Images were taken in five *z* sections (Δz=0.5 µm) with an excitation time of 80 ms and a laser intensity of 90%.

SIM

Imaging setup was as described in Rüthnick et al. (2017). In brief, Alexa Fluor 488–phalloidin-stained cells were suspended in PBS and imaged with an N-SIM system (Nikon, Tokyo, Japan) equipped with a total internal reflection fluorescence Apochromat 100×/1.49 NA oil immersion objective and a single-photon detection electron-multiplying charge-coupled device camera (iXon3 DU-897E; Andor Technology, Belfast, UK) using a 488 nm laser for excitation with an emission bandpass filter of 520/45. Reconstructions were performed with the image analysis software (Nikon). Images were taken in five *z* sections.

Quantitative analysis of fluorescence microscopy

All microscopy files were processed and analyzed with FIJI [version 2.0.0-rc-69; NIH (Schindelin et al., 2012)]. Images were acquired as five to 14 *z*-stacks and analyzed either in single layers or as projections of single layers.

The number of actin filaments running in parallel to the mother-bud axis within the bud or mother of yeast cells was determined with the assistance of the FIJI tool 'plot profile'. Filaments were counted at a position half way in the bud or half way in the mother compartment. Local intensity maxima were considered as actin filament counts. Quantification in the local enrichment of fluorescence intensity (RI, relative intensity) was calculated based on the formula:

$$\mathrm{RI} = (\mathrm{IROI} - \mathrm{IBackground})/(\mathrm{ICytosol} - \mathrm{IBackground}).$$

IROI describes the mean intensity within the region of interest (ROI); IBackground describes the mean intensity within a region outside of the cell; and ICytosol describes the mean intensity within a region of the cytosol of the mother compartment.

The ratio of the GFP–Sec4 intensities of the bud to the whole cell were calculated based on the formula:

$$[\text{Mean Intensity (ROI)} - \text{Mean Intensity (Background)}] \times \text{area (ROI)} / [\text{Mean Intensity (whole cell)} - \text{Mean Intensity (Background)}] \times \text{total area (whole cell)}.$$

To determine the local enrichment of GFP fusion proteins at peroxisomes, the mean intensity in the GFP channel at all mother-cell-located peroxisomes was averaged to determine IROI. The COV used to determine actin cable staining density was calculated as the ratio of s.d. to the mean fluorescence intensity of the whole mother cell or bud. Taking the

ratio of s.d. to the mean intensity enhances the sensitivity of measurement as both values correlate with the actin cable density (Garabedian et al., 2018). A less-dense actin cable network contains larger dark, cable-free regions. This results in a higher s.d. and a lower mean fluorescence intensity, thus increasing the COV.

The vesicle distribution in the bud of cells expressing GFP–Sec4 was determined from SIM images with the FIJI tool 'plot profile' by setting a ruler from the bud neck to the bud tip. The relative length was divided into 5% steps from 0% at the bud neck to 100% at the tip. Along this line (thickness, 0.16 µm=5 pixels), the mean fluorescence intensity was determined and the background subtracted. The mean intensities along this line represent relative intensities normalized to the highest mean intensity. Ten cells with bud lengths between 2 µm and 2.5 µm were analyzed for each genotype.

SIM image processing

Images were stacked to maximum projections. Background subtraction for the determination of actin cable numbers and actin cable staining density in bud and mother was performed with the 'running ball' method in FIJI with a radius of 20 pixels (=0.64 µm). To subtract the background for determination of the vesicle distribution in the bud, the highest intensity value in a vesicle-free cytosolic area of the mother was subtracted from all intensities in the bud.

To measure the relative fluorescence intensity of a certain region in the cell, the fraction of fluorescence intensity in the region of interest was calculated based on the formula:

$$[\text{Mean Intensity (ROI)} - \text{Mean Intensity (Background)}] \times \text{area (ROI)} / [\text{Mean Intensity (whole cell)} - \text{Mean Intensity (Background)}] \times \text{total area (whole cell)}.$$

Actin staining

Exponential-grown cells were fixed for 10 min by adding 3.7% formaldehyde to the medium. Cells were resuspended in 3.7% formaldehyde (in 100 mM KH_2PO_4) and incubated for 1 h before buffer was exchanged to 1 µM ethanolamine (in 100 mM KH_2PO_4) for 10 min. Cells were washed twice with PBS, and incubated with 66 nM Alexa-fluorophore-conjugated phalloidin (Thermo Fisher Scientific, Waltham, MA) for 30 min or overnight at 4°C. Actin patches were removed by addition of 100 µM CK-666 (Merck, Darmstadt, Germany) to the cell medium at 30°C, 10 min before cells were fixed. Samples that were imaged by SIM were prepared with buffers that were filtrated with a 0.22 µm syringe filter (#99722; TPP, Trasadingen, Switzerland) prior to usage.

Vesicle tethering analysis

Exponential-growing cells were embedded between a coverslip and a custom-made glass slide (Glassbläserei, Universität Ulm, Ulm, Germany) into a 3.8% agarose gel (containing 1× SD medium). Cells were imaged at room temperature (~22–26°C). To keep conditions constant among different genotypes, we measured the corresponding cells in a defined order and reversed this order during the repetition. To follow individual vesicles in the bud, images (five *z*-stacks, 0.5 µm per stack) were taken every second. Each time-lapse series included four images that were acquired before, and 100 images acquired after, bleaching the bud of the cell. Tethering time was determined as the time interval between the arrival of a vesicle at the cortex and the time when it disappears. Only vesicles were taken into account that stayed fixed for more than 4 s at the cortex and were visible in the middle three layers.

Vesicle distribution in the bud

To quantify the vesicle distribution of incoming vesicles in the bud over the whole time course of 100 images, the middle three layers were stacked to maximum projections. Maximum projections of the consecutive 100 images were further maximum projected into a single image. The mean intensity of a corridor below the plasma membrane of the bud was determined using the 'segmented line' tool in FIJI with a line width of 3 pixels (=0.326 µm), and normalized to the mean intensity of the whole bud. Both mean intensity values were background subtracted before calculating the ratio.

Vesicle-tracking analysis

Image acquisition

Yeast cells expressing GFP–Sec4 from a centromeric plasmid under a methionine adjustable P_{MET17} promoter were grown in selective medium lacking methionine. Exponentially grown cells were spun down and resuspended in selective medium. Then, 3.1 µl of the cell suspension was embedded between a glass microscopy slide and a cover slip. Microscopy was performed at room temperature. Images were taken with a confocal microscope over a time course of 35 s using a single *z*-stack and acquiring images every 100 ms (intensity of the 488 nm laser, 20%; excitation time, 50 ms). Before the start of each time lapse, an image of the green and red channel was taken to reconstruct the position of peroxisomes in the trajectory plots for post-analysis. The bud of the cells and vesicle-dense regions (in Pex–Boi1) in the cortex of the mother were subsequently bleached to increase the signal-to-noise ratio of single vesicles in the mother and daughter cell.

Vesicle tracking

Time-lapse images were analyzed with the MOSAIC suite plugin for Fiji/ImageJ (Sbalzarini and Koumoutsakos, 2005; Schindelin et al., 2012). To observe and follow vesicles over time, we adjusted the following parameters, whereas all other variables were left in default mode: for particle detection: particle radius, 0.133 µm; percentile (*r*), 0.3–1.5 (value was adjusted and vesicle detection was verified in randomly chosen images of the time lapse by using the 'preview detected' function). For particle linking: link range, five images; dynamics, Brownian; displacement, 1.33 µm/100 ms.

Directionality analysis

Directionality analysis based on microscopy coordinate measurements of trajectories was performed in R statistical package (R Core Team, 2013). For each cell, we first fitted a linear function delineating the mother cell and the bud. This function was later used to select trajectories originating from the mother cell for downstream directionality analyses. For each trajectory measured over a time span within a given cell, we calculated two Euclidean distance measurements: (1) distance between two subsequent time points, and (2) absolute Euclidean distance (displacement) from the original position. We then took the ratio of the net displacement to the cumulative distance travelled, with a maximum attainable upper limit value of 1 representing a perfectly directional trajectory moving in a straight line. For ease of interpretation, we took the log of this ratio, setting the maximum value to 0, so all variations of movement would fall in the negative range. In the final step, we measured area under the curve (AUC) of the calculated ratios along the entire length of the trajectory. To test the statistical significance of the directional movement against a random motion, we generated a null hypothesis distribution using a Monte Carlo simulation. To achieve this, coordinate measurements of each trajectory were first randomized and Euclidean and AUC measurements were calculated by following the steps discussed above. This was iterated 1000 times for each trajectory to finally generate the null distribution. Significance test of the empirical AUC was performed using the formula $P=(r+1)/(N+1)$, where N is the total number of iterations (1000), r is the number of events in the simulation model that yielded AUC values greater than the empirical or observed AUC, and P is the calculated P-value (Davison and Hinkley, 1997). The decision on whether a given trajectory was moving either towards or away from the bud was made strictly based on its final destination as determined by the linear function delimiting the mother cell and the bud. For final percentage of directional trajectories calculations, we excluded short trajectories with lengths less or equal to 9. Statistical comparisons of directionality measurements among genotypes was performed using the non-parametric Kruskal–Wallis one-way ANOVA followed by Dunn's pairwise post-hoc test.

Movement towards peroxisomes

To quantify the number of vesicles moving towards peroxisomes, we overlaid a plot containing vesicle destinations (generated with R) with an image of both fluorescent channels taken right before time-lapse microscopy. Peroxisomes at the mother cortex are mainly immobile,

allowing us to combine still images with subsequent time-lapse analysis (Fagarasanu et al., 2009). The directionality plot contained the destinations of vesicle trajectories that were calculated to move directional but away from the bud (not ending in the bud), and the destinations of all trajectories. The latter were required to overlay and correctly fit the proportions of the raw microscopy image with the directionality plot in order to locate the peroxisomes on each plot. We counted the number of trajectories moving away from the bud that colocalized or directly neighboring peroxisomal sites within each cell of a given allele.

Acknowledgements
We thank the Nikon Imaging Facility of the University of Heidelberg for granting access to SIM and its analysis; the Institute for General Physiology at Ulm University for providing introduction and access to the iMIC microscope; Ute Nussbaumer, Steffi Timmermann and Nicole Schmid for strain construction; and Drs Judith Müller, Alexander Dünkler and Reinhild Rösler for sharing constructs, advice and strains.

Competing interests
The authors declare no competing or financial interests.

Author contributions
Conceptualization: O.G., Y.W., N.J.; Methodology: O.G., M.A.M.; Software: O.G., M.A.M.; Validation: L.R.; Formal analysis: M.A.M.; Investigation: O.G., Y.W., L.R., D.R.; Writing - original draft: O.G., N.J.; Writing - review & editing: O.G., N.J.; Supervision: N.J.; Funding acquisition: N.J.

Funding
This work was funded by Deutsche Forschungsgemeinschaft [Jo 187/5-2 and Jo 187/8-1 to N.J.].

Supplementary information
Supplementary information available online at
http://jcs.biologists.org/lookup/doi/10.1242/jcs.237982.supplemental

References
Adamo, J. E., Moskow, J. J., Gladfelter, A. S., Viterbo, D., Lew, D. J. and Brennwald, P. J. (2001). Yeast Cdc42 functions at a late step in exocytosis, specifically during polarized growth of the emerging bud. *J. Cell Biol.* **155**, 581-592. doi:10.1083/jcb.200106065

Amberg, D. C., Zahner, J. E., Mulholland, J. W., Pringle, J. R. and Botstein, D. (1997). Aip3p/Bud6p, a yeast actin-interacting protein that is involved in morphogenesis and the selection of bipolar budding sites. *Mol. Biol. Cell* **8**, 729-753. doi:10.1091/mbc.8.4.729

Bender, L., Lo, H. S., Lee, H., Kokojan, V., Peterson, V. and Bender, A. (1996). Associations among PH and SH3 domain-containing proteins and rho-type GTPases in yeast. *J. Cell Biol.* **133**, 879-894. doi:10.1083/jcb.133.4.879

Bi, E. and Park, H.-O. (2012). Cell polarization and cytokinesis in budding yeast. *Genetics* **191**, 347-387. doi:10.1534/genetics.111.132886

Boyd, C., Hughes, T., Pypaert, M. and Novick, P. (2004). Vesicles carry most exocyst subunits to exocytic sites marked by the remaining two subunits, Sec3p and Exo70p. *J. Cell Biol.* **167**, 889-901. doi:10.1083/jcb.200408124

Brown, J. L., Jaquenoud, M., Gulli, M.-P., Chant, J. and Peter, M. (1997). Novel Cdc42-binding proteins Gic1 and Gic2 control cell polarity in yeast. *Genes Dev.* **11**, 2972-2982. doi:10.1101/gad.11.22.2972

Chasserot-Golaz, S., Vitale, N., Umbrecht-Jenck, E., Knight, D., Gerke, V. and Bader, M.-F. (2005). Annexin 2 promotes the formation of lipid microdomains required for calcium-regulated exocytosis of dense-core vesicles. *Mol. Biol. Cell* **16**, 1108-1119. doi:10.1091/mbc.e04-07-0627

Davison, A. C. and Hinkley, D. V. (1997). *Bootstrap Methods and their Application*. Cambridge: Cambridge University Press.

Donovan, K. W. and Bretscher, A. (2012). Myosin-V is activated by binding secretory cargo and released in coordination with rab/exocyst function. *Dev. Cell.* **23**, 769-781. doi:10.1016/j.devcel.2012.09.001

Donovan, K. W. and Bretscher, A. (2015). Tracking individual secretory vesicles during exocytosis reveals an ordered and regulated process. *J. Cell Biol.* **210**, 181-189. doi:10.1083/jcb.201501118

Dünkler, A., Müller, J. and Johnsson, N. (2012). Detecting protein-protein interactions with the split-ubiquitin sensor. *Methods Mol. Biol.* **786**, 115-130. doi:10.1007/978-1-61779-292-2_7

Evangelista, M., Blundell, K., Longtine, M. S., Chow, C. J., Adames, N., Pringle, J. R., Peter, M. and Boone, C. (1997). Bni1p, a yeast formin linking cdc42p and the actin cytoskeleton during polarized morphogenesis. *Science* **276**, 118-122. doi:10.1126/science.276.5309.118

Fagarasanu, A., Mast, F. D., Knoblach, B., Jin, Y., Brunner, M. J., Logan, M. R., Glover, J. N. M., Eitzen, G. A., Aitchison, J. D., Weisman, L. S. et al. (2009). Myosin-driven peroxisome partitioning in S. cerevisiae. *J. Cell Biol.* **186**, 541-554. doi:10.1083/jcb.200904050

Gabel, M., Delavoie, F., Demais, V., Royer, C., Bailly, Y., Vitale, N., Bader, M.-F. and Chasserot-Golaz, S. (2015). Annexin A2-dependent actin bundling promotes secretory granule docking to the plasma membrane and exocytosis. *J. Cell Biol.* **210**, 785-800. doi:10.1083/jcb.201412030

Garabedian, M. V., Stanishneva-Konovalova, T., Lou, C., Rands, T. J., Pollard, L. W., Sokolova, O. S. and Goode, B. L. (2018). Integrated control of formin-mediated actin assembly by a stationary inhibitor and a mobile activator. *J. Cell Biol.* **217**, 3512-3530. doi:10.1083/jcb.201803164

Graziano, B. R., DuPage, A. G., Michelot, A., Breitsprecher, D., Moseley, J. B., Sagot, I., Blanchoin, L. and Goode, B. L. (2011). Mechanism and cellular function of Bud6 as an actin nucleation-promoting factor. *Mol. Biol. Cell* **22**, 4016-4028. doi:10.1091/mbc.e11-05-0404

Graziano, B. R., Jonasson, E. M., Pullen, J. G., Gould, C. J. and Goode, B. L. (2013). Ligand-induced activation of a formin-NPF pair leads to collaborative actin nucleation. *J. Cell Biol.* **201**, 595-611. doi:10.1083/jcb.201212059

Guo, W., Roth, D., Walch-Solimena, C. and Novick, P. (1999). The exocyst is an effector for Sec4p, targeting secretory vesicles to sites of exocytosis. *EMBO J.* **18**, 1071-1080. doi:10.1093/emboj/18.4.1071

Guo, W., Tamanoi, F. and Novick, P. (2001). Spatial regulation of the exocyst complex by Rho1 GTPase. *Nat. Cell Biol.* **3**, 353-360. doi:10.1038/35070029

Hashizume, K., Cheng, Y.-S., Hutton, J. L., Chiu, C.-H. and Carr, C. M. (2009). Yeast Sec1p functions before and after vesicle docking. *Mol. Biol. Cell* **20**, 4673-4685. doi:10.1091/mbc.e09-02-0172

He, B., Xi, F., Zhang, X., Zhang, J. and Guo, W. (2007). Exo70 interacts with phospholipids and mediates the targeting of the exocyst to the plasma membrane. *EMBO J.* **26**, 4053-4065. doi:10.1038/sj.emboj.7601834

Hetrick, B., Han, M. S., Helgeson, L. A. and Nolen, B. J. (2013). Small molecules CK-666 and CK-869 inhibit actin-related protein 2/3 complex by blocking an activating conformational change. *Chem. Biol.* **20**, 701-712. doi:10.1016/j.chembiol.2013.03.019

Hruby, A., Zapatka, M., Heucke, S., Rieger, L., Wu, Y., Nussbaumer, U., Timmermann, S., Dünkler, A. and Johnsson, N. (2011). A constraint network of interactions: protein-protein interaction analysis of the yeast type II phosphatase Ptc1p and its adaptor protein Nbp2p. *J. Cell Sci.* **124**, 35-46. doi:10.1242/jcs.077065

Hume, A. N., Wilson, M. S., Ushakov, D. S., Ferenczi, M. A. and Seabra, M. C. (2011). Semi-automated analysis of organelle movement and membrane content: understanding rab-motor complex transport function. *Traffic* **12**, 1686-1701. doi:10.1111/j.1600-0854.2011.01283.x

Janke, C., Magiera, M. M., Rathfelder, N., Taxis, C., Reber, S., Maekawa, H., Moreno-Borchart, A., Doenges, G., Schwob, E., Schiebel, E. et al. (2004). A versatile toolbox for PCR-based tagging of yeast genes: new fluorescent proteins, more markers and promoter substitution cassettes. *Yeast* **21**, 947-962. doi:10.1002/yea.1142

Jin, Y., Sultana, A., Gandhi, P., Franklin, E., Hamamoto, S., Khan, A. R., Munson, M., Schekman, R. and Weisman, L. S. (2011). Myosin V transports secretory vesicles via a rab GTPase cascade and interaction with the exocyst complex. *Dev. Cell.* **21**, 1156-1170. doi:10.1016/j.devcel.2011.10.009

Johnsson, N. and Varshavsky, A. (1994). Split ubiquitin as a sensor of protein interactions in vivo. *Proc. Natl. Acad. Sci. USA* **91**, 10340-10344. doi:10.1073/pnas.91.22.10340

Jose, M., Tollis, S., Nair, D., Mitteau, R., Velours, C., Massoni-Laporte, A., Royou, A., Sibarita, J.-B. and McCusker, D. (2015). A quantitative imaging-based screen reveals the exocyst as a network hub connecting endocytosis and exocytosis. *Mol. Biol. Cell* **26**, 2519-2534. doi:10.1091/mbc.E14-11-1527

Kustermann, J., Wu, Y., Rieger, L., Dedden, D., Phan, T., Walther, P., Dünkler, A. and Johnsson, N. (2017). The cell polarity proteins Boi1p and Boi2p stimulate vesicle fusion at the plasma membrane of yeast cells. *J. Cell. Sci.* **130**, 2996-3008. doi:10.1242/jcs.206334

Laughery, M. F., Hunter, T., Brown, A., Hoopes, J., Ostbye, T., Shumaker, T. and Wyrick, J. J. (2015). New vectors for simple and streamlined CRISPR-Cas9 genome editing in saccharomyces cerevisiae. *Yeast* **32**, 711-720. doi:10.1002/yea.3098

Li, F. and Higgs, H. N. (2003). The mouse formin mDia1 is a potent actin nucleation factor regulated by autoinhibition. *Curr. Biol.* **13**, 1335-1340. doi:10.1016/S0960-9822(03)00540-2

Li, F. and Higgs, H. N. (2005). Dissecting requirements for auto-inhibition of actin nucleation by the formin, mDia1. *J. Biol. Chem.* **280**, 6986-6992. doi:10.1074/jbc.M411605200

Li, P., Bademosi, A. T., Luo, J. and Meunier, F. A. (2018). Actin remodeling in regulated exocytosis: Toward a mesoscopic view. *Trends Cell Biol.* **28**, 685-697. doi:10.1016/j.tcb.2018.04.004

Liu, D. and Novick, P. (2014). Bem1p contributes to secretory pathway polarization through a direct interaction with Exo70p. *J. Cell Biol.* **207**, 59-72. doi:10.1083/jcb.201404122

Luo, G., Zhang, J. and Guo, W. (2014). The role of Sec3p in secretory vesicle targeting and exocyst complex assembly. *Mol. Biol. Cell* **25**, 3813-3822. doi:10.1091/mbc.e14-04-0907

Masgrau, A., Battola, A., Sanmartin, T., Pryszcz, L. P., Gabaldón, T. and Mendoza, M. (2017). Distinct roles of the polarity factors Boi1 and Boi2 in the control of exocytosis and abscission in budding yeast. *Mol. Biol. Cell* **28**, 3082-3094. doi:10.1091/mbc.e17-06-0404

Meunier, F. A. and Gutiérrez, L. M. (2016). Captivating new roles of F-actin cortex in exocytosis and bulk endocytosis in neurosecretory cells. *Trends Neurosci.* **39**, 605-613. doi:10.1016/j.tins.2016.07.003

Morgera, F., Sallah, M. R., Dubuke, M. L., Gandhi, P., Brewer, D. N., Carr, C. M. and Munson, M. (2012). Regulation of exocytosis by the exocyst subunit Sec6 and the SM protein Sec1. *Mol. Biol. Cell* **23**, 337-346. doi:10.1091/mbc.e11-08-0670

Moseley, J. B. and Goode, B. L. (2005). Differential activities and regulation of saccharomyces cerevisiae formin proteins Bni1 and Bnr1 by Bud6. *J. Biol. Chem.* **280**, 28023-28033. doi:10.1074/jbc.M503094200

Moseley, J. B., Sagot, I., Manning, A. L., Xu, Y., Eck, M. J., Pellman, D. and Goode, B. L. (2004). A conserved mechanism for Bni1- and mDia1-induced actin assembly and dual regulation of Bni1 by Bud6 and profilin. *Mol. Biol. Cell* **15**, 896-907. doi:10.1091/mbc.e03-08-0621

Nakano, K., Toya, M., Yoneda, A., Asami, Y., Yamashita, A., Kamasawa, N., Osumi, M. and Yamamoto, M. (2011). Pob1 ensures cylindrical cell shape by coupling two distinct rho signaling events during secretory vesicle targeting. *Traffic* **12**, 726-739. doi:10.1111/j.1600-0854.2011.01190.x

Porat-Shliom, N., Milberg, O., Masedunskas, A. and Weigert, R. (2013). Multiple roles for the actin cytoskeleton during regulated exocytosis. *Cell Mol. Life Sci.* **70**, 2099-2121. doi:10.1007/s00018-012-1156-5

Pruyne, D. W., Schott, D. H. and Bretscher, A. (1998). Tropomyosin-containing actin cables direct the Myo2p-dependent polarized delivery of secretory vesicles in budding yeast. *J. Cell Biol.* **143**, 1931-1945. doi:10.1083/jcb.143.7.1931

R Core Team. (2013). *R: A Language and Environment for Statistical Computing. [computer program].* Vienna, Austria: R Foundation for Statistical Computing.

Rincón, S. A., Ye, Y., Villar-Tajadura, M. A., Santos, B., Martin, S. G. and Pérez, P. (2009). Pob1 participates in the Cdc42 regulation of fission yeast actin cytoskeleton. *Mol. Biol. Cell* **20**, 4390-4399. doi:10.1091/mbc.e09-03-0207

Rüthnick, D., Neuner, A., Dietrich, F., Kirrmaier, D., Engel, U., Knop, M. and Schiebel, E. (2017). Characterization of spindle pole body duplication reveals a regulatory role for nuclear pore complexes. *J. Cell Biol.* **216**, 2425-2442. doi:10.1083/jcb.201612129

Sbalzarini, I. F. and Koumoutsakos, P. (2005). Feature point tracking and trajectory analysis for video imaging in cell biology. *J. Struct. Biol.* **151**, 182-195. doi:10.1016/j.jsb.2005.06.002

Schindelin, J., Arganda-Carreras, I., Frise, E., Kaynig, V., Longair, M., Pietzsch, T., Preibisch, S., Rueden, C., Saalfeld, S., Schmid, B. et al. (2012). Fiji: An open-source platform for biological-image analysis. *Nat. Methods* **9**, 676-682. doi:10.1038/nmeth.2019

Schneider, C., Grois, J., Renz, C., Gronemeyer, T. and Johnsson, N. (2013). Septin rings act as a template for myosin higher-order structures and inhibit redundant polarity establishment. *J. Cell Sci.* **126**, 3390-3400. doi:10.1242/jcs.125302

Sheu, Y.-J., Santos, B., Fortin, N., Costigan, C. and Snyder, M. (1998). Spa2p interacts with cell polarity proteins and signaling components involved in yeast cell morphogenesis. *Mol. Cell. Biol.* **18**, 4053-4069. doi:10.1128/MCB.18.7.4053

Sikorski, R. S. and Hieter, P. (1989). A system of shuttle vectors and yeast host strains designed for efficient manipulation of DNA in saccharomyces cerevisiae. *Genetics* **122**, 19-27.

Storici, F. and Resnick, M. A. (2006). The delitto perfetto approach to in vivo site-directed mutagenesis and chromosome rearrangements with synthetic oligonucleotides in yeast. *Methods Enzymol.* **409**, 329-345. doi:10.1016/S0076-6879(05)09019-1

Sudhof, T. C. and Rothman, J. E. (2009). Membrane fusion: Grappling with SNARE and SM proteins. *Science* **323**, 474-477. doi:10.1126/science.1161748

Takahashi, S. and Pryciak, P. M. (2007). Identification of novel membrane-binding domains in multiple yeast Cdc42 effectors. *Mol. Biol. Cell* **18**, 4945-4956. doi:10.1091/mbc.e07-07-0676

Tcheperegine, S. E., Gao, X.-D. and Bi, E. (2005). Regulation of cell polarity by interactions of Msb3 and Msb4 with Cdc42 and polarisome components. *Mol. Cell. Biol.* **25**, 8567-8580. doi:10.1128/MCB.25.19.8567-8580.2005

Tu, D., Graziano, B. R., Park, E., Zheng, W., Li, Y., Goode, B. L. and Eck, M. J. (2012). Structure of the formin-interaction domain of the actin nucleation-promoting factor Bud6. *Proc. Natl. Acad. Sci. USA* **109**, E3424-E3433. doi:10.1073/pnas.1203035109

Umbrecht-Jenck, E., Demais, V., Calco, V., Bailly, Y., Bader, M.-F. and Chasserot-Golaz, S. (2010). S100A10-mediated translocation of annexin-A2 to SNARE proteins in adrenergic chromaffin cells undergoing exocytosis. *Traffic* **11**, 958-971. doi:10.1111/j.1600-0854.2010.01065.x

Wittke, S., Lewke, N., Müller, S. and Johnsson, N. (1999). Probing the molecular environment of membrane proteins in vivo. *Mol. Biol. Cell* **10**, 2519-2530. doi:10.1091/mbc.10.8.2519

Wu, H., Turner, C., Gardner, J., Temple, B. and Brennwald, P. (2010). The Exo70 subunit of the exocyst is an effector for both Cdc42 and Rho3 function in polarized exocytosis. *Mol. Biol. Cell* **21**, 430-442. doi:10.1091/mbc.e09-06-0501

Yamashita, M., Kurokawa, K., Sato, Y., Yamagata, A., Mimura, H., Yoshikawa, A., Sato, K., Nakano, A. and Fukai, S. (2010). Structural basis for the rho- and phosphoinositide-dependent localization of the exocyst subunit Sec3. *Nat. Struct. Mol. Biol.* **17**, 180-186. doi:10.1038/nsmb.1722

Yue, P., Zhang, Y., Mei, K., Wang, S., Lesigang, J., Zhu, Y., Dong, G. and Guo, W. (2017). Sec3 promotes the initial binary t-SNARE complex assembly and membrane fusion. *Nat. Commun.* **8**, 14236. doi:10.1038/ncomms14236

Zhang, X., Bi, E., Novick, P., Du, L., Kozminski, K. G., Lipschutz, J. H. and Guo, W. (2001). Cdc42 interacts with the exocyst and regulates polarized secretion. *J. Biol. Chem.* **276**, 46745-46750. doi:10.1074/jbc.M107464200